

ZURICH UNIVERSITY OF APPLIED SCIENCES  
DEPARTMENT LIFE SCIENCES AND FACILITY MANAGEMENT  
IUNR INSTITUTE OF NATURAL RESOURCE SCIENCES

---

**Quantitative assessment of terrestrial sediment budgets in a  
hydropower-regulated floodplain using point cloud classification**

---

MASTER THESIS  
GUBELMANN YVES

MASTER STUDIES IN ENVIRONMENT AND NATURAL RESOURCES  
SPECIALIZATION IN BIODIVERSITY AND ECOSYSTEMS

June 29, 2023

SUPERVISORS:

PROF. DR. DÖRING MICHAEL<sup>A</sup>, DR. ANTONETTI MANUEL<sup>A</sup>, DR. JOHANN JUNGHARDT<sup>B</sup>

<sup>A</sup>Ecohydrology Research Group, Institute of Natural Resource Sciences, Zurich University of Applied Sciences,  
Grüentalstrasse 14, 8820 Wädenswil, Switzerland

<sup>B</sup>Geoinformatics Research Group, Institute of Natural Resource Sciences, Zurich University of Applied Sciences,  
Grüentalstrasse 14, 8820 Wädenswil, Switzerland

## Impressum

**Author**

Yves Gubelmann

**Keywords**

Cloth Simulation Filter  
Terrestrial Laser Scanner  
Airborne Structure-from-Motion  
Spatial R  
LidR  
Artificial floods

**Citation**

Gubelmann, Y (2023). Quantitative assessment of terrestrial sediment budgets in a hydropower-regulated floodplain using point cloud classification. (Master Thesis). Ecohydrology Research Group, Zurich University of Applied Sciences.

**Institute**

Institute of Natural Resource Sciences  
Zurich University of Applied Sciences  
Grüentalstrasse 14  
8820 Wädenswil, Switzerland

**Correspondence to**

yves.gubelmann@gmx.ch

## Abstract

Sediment budgeting is an established method to assess spatiotemporal volumetric changes of erosion and deposition along gravel-bed rivers. Especially along hydropower-regulated rivers, sediment budgeting allows the volumetric impact caused by artificial floods to be quantified and provides valuable information to estimate their positive impact on the ecosystem. To date, this has been achieved with cumbersome survey techniques and labor-intensive post-processing. Recent advances in remote sensing allow the acquisition of high-resolution point cloud data in less time and on network scale level. This master thesis presents a workflow in which common sediment budgeting was further developed using point cloud classification and applied on a densely vegetated and hydropower-regulated floodplain in the pre-alpine Sarine River. Prior to the budget calculation, cloth simulation filter (CSF) was tested for the automated point cloud classification of sediment and water bodies. Sediment point clouds with the highest agreement compared to a reference data set were used for sediment budgeting. Furthermore, the point cloud uncertainties were measured and propagated into the sediment budget with a confidence interval of 95%. With the developed workflow, point clouds acquired by a terrestrial laser scanner (TLS) were compared with point clouds derived from airborne Structure-from-motion (UAV-SfM) to investigate added value of TLS technique. Furthermore, sediment budgets of three flood events were calculated based on UAV-SfM point clouds and used to investigate the quantitative effects on erosion and deposition. Compared to the reference data, the water bodies derived from CSF classification showed substantial agreement, whereas sediment classification showed slightly lower agreement. Additionally, TLS-based classifications identified terrestrial sediment areas below overhanging vegetation which was overseen with UAV-based classifications. The measured surface uncertainties of UAV data resulted in a critical level of detection of  $\pm 0.15$  m which is in alignment with similar studies, while TLS failed to achieve smaller levels due to georeferencing errors. Two of three obtained sediment budgets achieved a reasonable loss of discarded volumes, whereas the smallest flood showed a significant number of discarded volumes. However, elevation change distribution (ECD) of each flood showed a unique and plausible geomorphic signature. It was concluded that: (i) the different agreement scores derived from sediment and water classification resulted from low point density and fragmented sediment bodies (for UAV data) and lacking suitability of CSF for the terrestrial perspective (for TLS), (ii) added value was observed for TLS when applied in small-scale river sections where overhanging vegetation covers sediment, (iii) minor floods exhibited an erosion-dominant character, whereas the largest investigated flood showed a pronounced deposition of sediment, that was mobilized upstream and transported to the floodplain. The developed workflow provides a scalable, computer efficient and accessible tool for sediment budgeting but requires further testing on network-scale gravel-bed rivers. However, it entails the potential of supporting river management and is built for the implementation of upcoming point cloud classification features.

## Acknowledgement

THIS THESIS WAS ONLY POSSIBLE THANKS TO VARIOUS SUPPORTERS. PRIMARILY, MY PROFOUND APPRECIATION GOES TO MY SUPERVISORS DR. MANUEL ANTONETTI FROM THE ZURICH UNIVERSITY FOR APPLIED SCIENCES (ZHAW), PROF. DR MICHAEL DÖRING AND DR. JOHANN JUNGHARDT FROM ZHAW. A SPECIAL THANK GOES TO MANUEL ANTONETTI. I HIGHLY APPRECIATED YOUR SUPPORTIVE MANNER, YOUR VALUABLE FEEDBACK AND YOUR BROAD KNOWLEDGE ABOUT ECOHYDROLOGY. IT WAS HIGHLY APPRECIATED DURING THE ENTIRE PROCESS. I ALSO WANT TO THANK DR MICHAEL DÖRING FOR MAKING THIS TOPIC POSSIBLE. DEVELOPING A R SCRIPT FOR AN RELEVANT HYDROLOGICAL APPLICATION MOTIVATED ME STRONGLY. FURTHERMORE, I WANT TO EXTEND MY GRATITUDE TO ALL MEMBERS OF THE ECOHYDROLOGY RESEARCH GROUP AT THE ZHAW. THANK YOU FOR SHARING YOUR WORKSPACE WITH ME AND THE INTERESTING DISCUSSION AT LUNCH TIME.

I ALSO WANT TO EXPRESS MY APPRECIATION TO THE GEOINFORMATICS RESEARCH GROUP. WITHOUT THE GENEROUS ACCESS TO THEIR COMPUTATIONAL INFRASTRUCTURE ANY POINT CLOUD CLASSIFICATION ROUTINE WOULD NOT BE FINISHED YET. SPECIAL THANKS GOES TO DR. JOHANN JUNGHARDT FOR THE INTRODUCTION INTO POINT CLOUDS AND PROVIDING AN IDEA OF A POSSIBLE APPROACH. LIKEWISE, I WOULD LIKE TO THANK NILS RATNAWEERA AND JOEL VON ROTZ FOR THE CODING ADVICE. NILS, YOU ENABLED ME TO WRITE THIS DOCUMENT WITH QUARTO AND JOEL PROVIDED APPROPRIATE QUARTO SUPPORT WHEN NEEDED.

FURTHERMORE, I WANT TO EXPRESS MY GREAT APPRECIATION TO MY PARENTS WHO ALWAYS SUPPORTED ME DURING MY EDUCATION AND PROVIDED A WARM WORKING ENVIRONMENT AT HOME. FINALLY, I WANT TO THANK MAXIMILIAN LEDERER AND MY PARTNER, TATJANA WAIS, FOR PROOFREADING, YOUR EMOTIONAL SUPPORT AND STEADY CONFIDENCE IN ME.

# Content

<b>1</b>	<b>Introduction</b>	<b>5</b>
1.1	Sediment budget as indicator of mitigation measure efficiency . . . . .	5
1.2	Common sediment budget assessments and alternatives . . . . .	5
1.3	Dealing with uncertainties in digital elevation models of difference . . . . .	6
1.4	Automated classification of sediment points in a point cloud . . . . .	6
1.5	Research questions . . . . .	7
<b>2</b>	<b>Data and methods</b>	<b>8</b>
2.1	Study area . . . . .	8
2.2	Properties of flood events 2020, 2021 and 2022 . . . . .	9
2.3	Airborne photogrammetry samples . . . . .	9
2.4	Terrestrial laser scanning samples . . . . .	9
2.5	Generation of point cloud data . . . . .	10
2.6	Pre-processing dense point clouds . . . . .	10
2.7	CSF classification routine . . . . .	11
2.7.1	Parameter optimization . . . . .	12
2.8	Sediment Budget . . . . .	12
<b>3</b>	<b>Results</b>	<b>16</b>
3.1	Automated classification of sediment and water bodies . . . . .	16
3.2	Added value of sediment budgets derived from TLS data . . . . .	19
3.3	Impact of flood events 2020, 2021 and 2022 on terrestrial sediment volumes . . . . .	21
3.3.1	Spatiotemporal distribution of terrestrial sediment habitats . . . . .	21
3.3.2	Estimation of surface representation uncertainty . . . . .	21
3.3.3	Calculation of sediment budgets . . . . .	21
<b>4</b>	<b>Discussion</b>	<b>27</b>
4.1	Automated classification of sediment and water bodies . . . . .	27
4.2	TLS for complex and densely vegetated floodplains . . . . .	28
4.2.1	Accurate TLS surface representation remains a challenge . . . . .	28
4.3	Sediment budgets derived from UAV-SfM point clouds . . . . .	28
4.3.1	Quantitative effects of the floods 2020, 2021 and 2022 . . . . .	28
4.3.2	Probabilistic uncertainty assessments with UAV-SfM data . . . . .	29
4.3.3	2D habitat change map as intermediate result . . . . .	29
4.3.4	Significance assessment of propagated uncertainty . . . . .	29
<b>5</b>	<b>Conclusion and Outlook</b>	<b>30</b>
<b>References</b>		<b>32</b>
<b>Appendix</b>		<b>38</b>

# 1 Introduction

Floodplains are highly dynamic ecosystems which provide habitats for a wide range of species (Bunn & Arthington, 2002; Maddock et al., 2013). Driven by variation in disturbances such as droughts and floods (Tockner et al., 2008), these abiotic processes lead to occasional morphological changes along a riverine system. The rearrangement of sediments in form of erosion and deposition is one mechanism which contributes the renewal process of a vital riverine ecosystem (Thorp et al., 2008; Ward & Stanford, 1983).

The construction of dams for hydropower production and increasing pressure by different forms of land-use threaten these riverine ecosystems dramatically (Tockner et al., 2008). Hydropower production, in particular, impact river sections directly downstream the dam (referred to as residual flow sections) in various ways. It not only restricts the longitudinal connectivity, sediment transport and pioneer floodplain habitats (Tonolla et al., 2021) but also increases colmation (i.e. clogging of sediment). Lacking bedload dynamics and restricted morphological change in residual flow sections result in decreased habitat availability not only for fish and invertebrates (Bunn & Arthington, 2002). Mitigation measures are required to lessen these consequences for the ecosystem (Habersack et al., 2013; Tonolla et al., 2021; Zurwerra et al., 2016). In Switzerland, the Waters Protection Act lists mitigation measures along residual flow sections as legal obligation (SR 814.20 - Federal Act of 24 January 1991 on the Protection of Waters, 2023).

One mitigation measure are artificial floods, namely when a storage hydropower production plant releases water from the dam into the residual flow section. It imitates a natural flood event and aims at the reactivation of riverine dynamics (Zurwerra et al., 2016). Depending on the magnitude and duration of such a single disturbance, sediment is relocated, colmation is reduced and overtaking vegetation is restricted (Döring et al., 2018; Stähly et al., 2019; Tonolla et al., 2021). Artificial floods along the Spöl River, an alpine river in the Swiss National Park, showed that repeated annual flood events had a positive effect on the invertebrate communities and reduced colmation (Kastenhofer, 2022; Robinson et al., 2018).

## 1.1 Sediment budget as indicator of mitigation measure efficiency

Besides the positive ecological effects of an artificial floods, the release of unused potential energy also causes a distinct financial loss for hydropower providers. Therefore, these stakeholders are interested in accounting the effect which builds the basis for effective measures. The assessment of a sediment budget is an approach which is capable to fulfill these interests. When records are taken before and after a flood, this quantitative method allows to: (i) identify erosion and deposition of sediment and (ii) estimate the volume change caused by the flood (Lane et al., 2003; Wheaton et al., 2009). Not only hydropower providers are interested in such assessments. Sediment transport rates (here volume over time) provide key input parameters for numerical modelling in ecohydrology (Flükiger, 2022; Habersack et al., 2013; Lane et al., 2020), since their direct measurement remains a challenge (Habersack et al., 2013; Schwindt et al., 2023; Warrick et al., 2015). Furthermore, the spatiotemporal character of such assessments provides useful information about fluvial morphological change and therefore an ideal method for repeated topographic surveys (Brewer & Passmore, 2002; Croke et al., 2013; Lane et al., 2003; Wheaton et al., 2009) or studies of dam removal campaigns (Warrick et al., 2015).

## 1.2 Common sediment budget assessments and alternatives

Depending on the spatial scale, time period and desired accuracy, different approaches have been used to obtain a sediment budget: (i) quantify sediment fluxes (Hoffmann et al., 2007; Houben et al., 2006; Warrick et al., 2015), (ii) by observing soil types and their residence time (Berendsen et al., 2001; Macaire et al., 2006) or using pedogenetic properties at sites where soils built an uniform pattern over large extents (Ganssen & Gračanin, 1972). A well-established sediment budgeting approach (Brown et al., 2009) is based on digital elevation models of difference (DoD). Along the investigated area, a digital elevation model (DEM) is generated for each topographic observation (Brown et al., 2009). The calculated difference between two observations results in a DoD which exhibits the elevation change of the investigated area. Originally, such DEMs have been acquired by RTK-GPS (Brasington et al., 2000), total stations (Milne & Sear, 1997; Wheaton et al., 2009) or airborne photogrammetry

(Westaway et al., 2001), resulting in labor-intensive field campaigns. With light detection and ranging (LiDAR) and terrestrial laser scanning (TLS) two remote sensing technologies have emerged (Cavalli et al., 2008; Croke et al., 2013; Eltner et al., 2013; Milan et al., 2007; Thoma et al., 2005) which are able to produce unprecedented volumes of georeferenced observations with sub-centimeter accuracy in even less time (Brasington et al., 2012). For each observation, these airborne or ground-based instruments emit a light pulse and measure travel time and intensity of the reflected pulse (National Ecological Observatory Network, 2023). Such records can be enriched with RGB information and then displayed as a point cloud, representing a virtual duplicate of the scenery.

As alternative, Structure-from-Motion (SfM), a sophisticated image reconstruction approach, challenges costly laser scanners. With SfM, ordinary camera images are used for point cloud generation which then can be applied in various topographic surveys. SfM data has already been applied for soil erosion assessments (Clapuyt et al., 2017; Eltner et al., 2015; Malinowski et al., 2023), tree segmentation (Schilling, 2023), morphological change detection along glaciers (Ely et al., 2017; Westoby et al., 2020), agricultural areas (Hunt & Daughtry, 2018) and hydrological applications (Lane et al., 2020; Mandlburger et al., 2015; Woodget et al., 2015). With regard to sediment budgets, SfM has also been applied on coasts (Callow et al., 2018; Carvalho & Reef, 2022; Rotnicka et al., 2020) or on gravel-bed rivers with none or spare vegetation (Conesa-García et al., 2020; Dai et al., 2022; Lane et al., 2020) but barely on densely vegetated floodplains.

### 1.3 Dealing with uncertainties in digital elevation models of difference

Depending on the scale of the investigated area, used acquisition and post-processing methods, point cloud measurements show errors in surface elevations ranging from  $\pm 0.0013$  m to  $\pm 3$  m (Eltner et al., 2016; Hodge et al., 2009; Rotnicka et al., 2020; Wheaton et al., 2009). As natural disturbances like flood events can lead to elevation changes of similar magnitude to this noise, uncertainty assessment becomes a crucial aspect of sediment budgeting. Brasington et al. (2003) and Lane et al. (2003) proposed a probabilistic uncertainty assessment method, which allows to identify a critical level of detection where elevation changes cannot be distinguished from noise. It is based on an error assessment of each DEM which then is propagated into the DoD, where uncertain elevation changes are discarded from the sediment budget. This approach is successfully applied with sensors like total stations (Wheaton et al., 2009), airborne LiDAR (Croke et al., 2013; Lane et al., 2003; Mandlburger et al., 2015) and TLS (Milan et al., 2007). On the one hand, recent advances in Uncrewed Aerial Vehicles (UAV) and post-processing technologies like SfM deliver promising point densities for network scale surveys (Eltner et al., 2016; Westoby et al., 2012). Whether UAV-SfM point clouds suit the requirements to quantify a sediment budget with a reasonable surface representation level is questionable. On the other hand, in the context of a densely vegetated floodplain, TLS might deliver added value as well. For instance, TLS provides sub-centimeter accuracy (Hodge et al., 2009) resulting in decreasing surface representation uncertainty. Although considerable attention has been paid on sediment budgeting either based on UAV or TLS data, rather less research has been devoted to a comparison of these different techniques.

### 1.4 Automated classification of sediment points in a point cloud

The classification of ground and water bodies becomes a crucial step in the workflow of sediment budgeting. Image-based hydromorphological surveys use artificial neural networks (Casado et al., 2015), supervised (Scheib, 2022) or index-based (Sivanpillai & Miller, 2010) classification for this task. Such two dimensional approaches are effective for flat, none-vegetated river sections but do not suit complex areas where overhanging objects like trees or cliffs hinder an effective classification (Casado et al., 2015). This issue can be countered with point cloud data. Topographic surveys with a focus on water differentiation between land and water bodies effectively use the returned signal intensity (Höfle et al., 2009; Legleiter, 2012; Morsy, 2017; Sangireddy, 2011), point density (Lang & McCarty, 2009) or multi-spectral indices (Morsy et al., 2016). In other disciplines derived point metrics (Yu et al., 2010; K. Zhang et al., 2003; W. Zhang et al., 2016) are already applied to differentiate between ground and none-ground points (see Table 1). Especially the Cloth Simulation Filter (CSF) developed by W. Zhang et al. (2016) represents a powerful tool (Bailey et al., 2022) has been successfully applied in forest management applications like tree segmentation (Brieger et al., 2019; Schilling, 2023). CSF simulates the physical behavior of rigid cloth, which is dropped on a rotated surface. After the cloth is dropped, all touched surfaces are classified

as ground. CSF offers an effective alternative when an additional signal (for instance intensity) is not available. It can be identified that classification of land and water bodies based on point-metrics is well investigated, but the classification of sediment and water bodies with CSF lacks testing. Therefore, a focus is set there.

Table 1: Different methods for the differentiation of ground bodies ordered by data source, classification method, target bodies and source.

Data	Classification Method	Target bodies	Source
LiDAR	Intensity signal	Land - Water	Höfle et al. (2009)
		Land - Water	Legleiter (2012)
		Land - Water	Morsy (2017)
		Land - Water	Sangireddy (2011)
	Multi-spectral indices	Land - Water	Morsy et al. (2016)
		Land - Water	Lang & McCarty (2009)
		Point metrics	Yu et al. (2010)
	CSF	Ground - Building	K. Zhang et al. (2003)
		Ground - Nonground	W. Zhang et al. (2016)
		Ground - Vegetation	Bailey et al. (2022)
		Ground - Trees	Schilling (2023)
		Ground - Trees	Brieger et al. (2019)
RGB Orthophoto	Artificial Neural Network Supervised Classification Indices	Sediment - Water	Casado et al. (2015)
		Sediment - Water	Scheib (2022)
		Land - Water	Sivanpillai & Miller (2010)

## 1.5 Research questions

The main objective of this master thesis focused on the development and application of a workflow to estimate sediment budgets based on point cloud data. Sediment budgeting is established along gravel-bed rivers or coastal areas but lack application along a densely vegetated floodplain. Within such complex riverine environments, an effective classification of sediment bodies is essential. Like other ground classification approaches based on point metrics, CSF provide high accuracy but remains untested for the classification of sediment and water bodies. Furthermore, it was hypothesized that the use of TLS data for sediment budgeting in a densely vegetated floodplain would provide added value due significant higher resolution. With the developed workflow, terrestrial sediment volumes of three flood events (in 2020, 2021 and 2022) are quantified and can be investigated. Finally a third focus is set on the quantified impact which also allows the magnitude and duration of each flood to be compared.

Given the identified research gaps, the following three research questions were addressed:

1. Can Cloth Simulation Filter (W. Zhang et al., 2016) achieve satisfactory results when used as a classification tool for water surface and terrestrial sediment?
2. What is the added value for quantitative assessment of sediment budgets when using TLS instead of UAV?
3. What are the quantitative effects of the floods 2020, 2021 and 2022 on erosion and deposition of terrestrial sediment volumes which can be estimated based on point cloud classification?

## 2 Data and methods

### 2.1 Study area

The study area is a section of the Sarine River, a pre-alpine river located in Western Switzerland (Figure 1). The Sarine River sources in the Valaisian Alps and flows through the Cantons of Valais, Vaud, Fribourg and Berne, joins the Aare River and flows then into the Rhine River. Till the Sarine River joins the Aare River its longitudinal continuum is disrupted six times by hydropower production, resulting in a restricted flow regime (Flükiger, 2022). The investigated area is located between the Rossens dam, which ponds the Lake of Gruyère and the Hauterive power station. This long residual flow section meanders with an average gradient of 0.3 % (Stähly et al., 2019) and is characterized by pool and riffle sequences. The investigated area can be described as engraved canyon-like river accompanied by overhanging vegetation along the shores. At the inner reach of the meander an island with an active side channel can be found. An 1000 m long section of the river was surveyed with an UAV, an 260m long section with an TLS (Figure 1). Upstream and downstream the island two inactive side channels are present which are reactivated eventually during a flood.

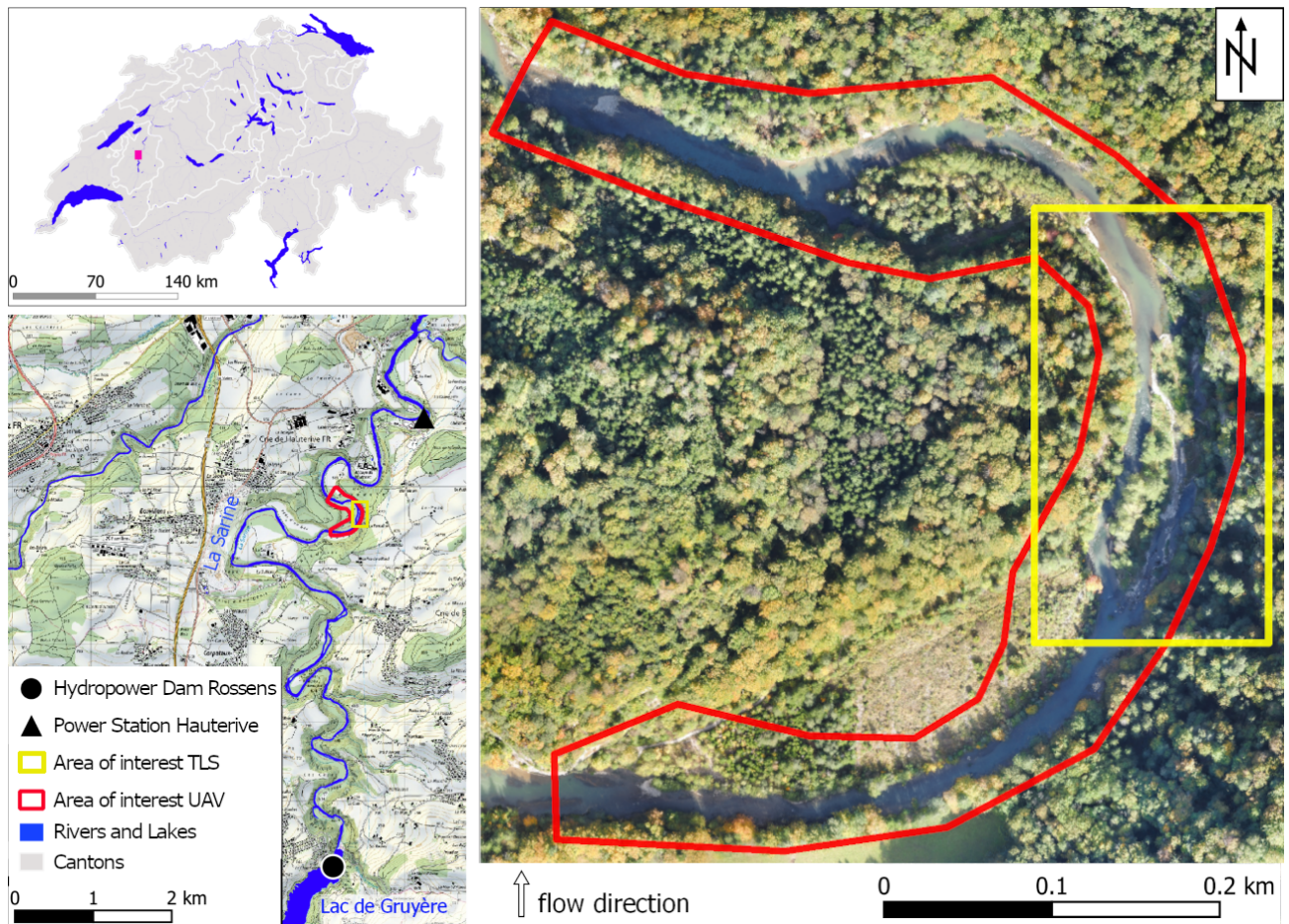


Figure 1: The investigated area, showing the area of interest covered by UAV (red) and covered by TLS (yellow). (Source: swissTLM3D and Swiss Map Raster 25 Federal Office of Topography swisstopo (2023), Orthoimage before the flood event on the 8.10.2020 provided by the Ecohydrology research group).

## 2.2 Properties of flood events 2020, 2021 and 2022

The investigated flood events differ in duration, intensity and discharged volume (Table 2). In 2020, an artificial flood with an maximum discharge of 112.5 m<sup>3</sup>/s and a duration of 22 hours was released. Heavy and enduring rain events in summer 2021 led to a release of 72.3 Mio. m<sup>3</sup> over 212 hours (8.8 days) with a maximum discharge of 302.2 m<sup>3</sup>/s. The smallest flood event during the investigated period took place in 2022, when a volume of 1.3 Mio m<sup>3</sup> was released over 13 hours with a discharge of 75 m<sup>3</sup>/s. In contrast to prior events (Stähly et al., 2019), no sediment replenishment was placed during these events. Apart from the flood in 2020, discharge records were provided by the hydropower station (otherwise provided by the Ecohydrology research group, marked with \*).

Table 2: Properties of flood events within investigated area showing date, duration, maximum and minimum discharge, as well as total discharged volume. Data provided by hydropower station, otherwise by Ecohydrology research group (marked with \*).

Date	Event	Duration	Maximum Discharge	Discharged Volume
22.10.2020	artificial flood	22	112.5*	6.6
11.-19.7.2021	natural flood	212	302.3	72.3
31.5.2022	minor artificial flood	13 [h]	75 [m <sup>3</sup> /s]	1.3 [Mio. m <sup>3</sup> ]

## 2.3 Airborne photogrammetry samples

The SfM point cloud is based on surveys conducted with the drones Wingtra One RX1R ll from Wingtra and eBee Plus from SenseFly (Table 3). The Wingtra One carries a 42 Megapixel camera with a metric 50 mm lens, whereas the eBee Plus has a 20 Megapixel camera with a metric 29 mm lens. The platforms support post-processed kinematic (PPK) which allows sub-decimeter accuracy. The samples were taken in October and early November (Table 3) to ensure identical phenological stages of the vegetation. Additionally, the flights were executed during midday to reduce large areas covered by shadows. Flights with the eBee yielded an average ground sampling distance (GSD) of 6.50 cm (8.10.2020) and 6.62 cm (5.11.2020) whereas the Wingtra One yielded 2.5 cm (14.10.2021) and 2.32 cm (7.10.2022). For georeferencing, between 4 to 14 ground control points (GCP) were used. In 2022, for an uncertainty assessment, similar to Woodget et al. (2015), additional 17 validation targets were placed in a random order and surveyed with a RTK-GPS (Trimble R10 GNSS system; accuracy < 0.02 m in horizontal and < 0.05 m in vertical direction, Trimble Incorporated (2021)).

## 2.4 Terrestrial laser scanning samples

The TLS point cloud was acquired with RIEGL VZ-1000 with an additional NIKON D700 camera on it. The eye-safe (class 1) laser was employed to acquire the terrestrial topography since the laser wavelength is not water penetrating. Simultaneously to the scan, the calibrated NIKON D700 camera (mounted on top) took pictures of the scenery. The laser recorded full 360° scans from 14 different locations. Careful positioning of the scanners reduced line of sight losses due to vegetation and shadowing. For georeferencing and co-registration, 6 reference spheres were placed. In 2022, the same validation targets were used for an uncertainty assessment.

Table 3: Point cloud data used for testing the developed workflow, including acquisition date, carrier platform, sensor, ground sampling distance (GSD) and point density. As carrier platform, either airborne photogrammetry (Wingra One or eBee Plus) or terrestrial laser scanning (RIEGL VZ-1000) was used.

Date	Carrier platform	Sensor	GSD	Point density
8.10.2020	eBee Plus	S.O.D.A. 10.6 (5472x3648 px)	6.5	34.39
5.11.2020	eBee Plus	S.O.D.A. 10.6 (5472x3648 px)	6.62	32.21
13.10.2021	TLS	RIEGL VZ-1000	NA	12461
14.10.2021	Wingtra One	DSC-RX1RM2 35.0 (7952x530 px)	2.50	184.02
7.10.2022	Wingtra One	DSC-RX1RM2 35.0 (7952x530 px)	2.32	206.37
11.10.2022	TLS	RIEGL VZ-1000	NA	13956
			[cm/Pixel]	[points/m <sup>2</sup> ]

## 2.5 Generation of point cloud data

The UAV images were used to reconstruct a georeferenced point cloud. This was done with the SfM algorithm of Pix4Dmapper Pro (Pix4D S.A., 2023). This reconstruction algorithm automatically ties keypoints of overlapping images together. To gain a high accuracy, post-processed kinematic (PPK) and GCPs were used for the geometric correction of the images (Westoby et al., 2012). A densified point cloud with a point density of >32 points/m<sup>2</sup> for the eBee and >184 points/m<sup>2</sup> for the WingtraOne was retrieved (Table 3). The TLS data was processed with RiScan Pro (RIEGL Laser Measurement Systems GmbH, 2023). The 14 point cloud, one each scan position, were colorized with their respective photos. After the color enrichment the scan positions were co-registered and georeferenced with reference spheres or GCPs. Finally, dense point cloud clouds with a point density of >12000 points/m<sup>2</sup> were retrieved. All point cloud datasets were provided by the Ecohydrology research group. Additionally, shapefiles of water and sediment bodies were provided by the Ecohydrology research group. These two dimensional bodies were used as reference to test intermediate results derived from CSF classification (research question Nr. 1). The data originates from a supervised pixel-based random forest classification and has been successfully used as validation data in prior studies (Scheib, 2022).

## 2.6 Pre-processing dense point clouds

Prior to classification of water and sediment bodies, dense point clouds were pre-processed to exclude not relevant points from the point cloud (TLS point clouds only). This step was carried out to: (i) reduce the workload of following expensive computational steps, (ii) minimize mid-air observations, which would distort further processing and (iii) compare only identical extents to ensure a consistent comparison between two timesteps (Lane et al., 2003).

First, the point cloud (.las-file) was loaded with the lidR package (Roussel et al., 2020) and points outside of the area of interest (.shp-file) or without RGB information were excluded from the point cloud. Next, mid-air observations such as dust or insects were removed by a statistical outlier removal (SOR). This function computes the mean distance to all its k-nearest neighbors for each point. Points which are farther away than the average distance plus a five times the standard deviation (nSigma) were discarded from the point cloud (cloudcompare.org, 2023). This threshold value was set after testing a range of different distance values (3 to 8 at 1.0 intervals).

After the SOR filtering, an RGB-based filter was applied. The RGB attributes excess blue index (ExB) and RGB mean were calculated as 16-bit integer (range: 0 - 65535) for each point. The attributes are based solely on the RGB information and require no derived metrics from neighboring points. With RGB mean, black and white points were excluded from the point cloud since, from a certain level on, such points cannot be classified by their color anymore. Furthermore, with ExB sky points, which are irrelevant for a sediment budget, could be identified. The specific threshold of each class (black, white and sky points) was determined beforehand in an

iterative process based on visual inspection. The following conditions were applied on every point in the listed order:

- **Noise** (mid-air observations): SOR with 25 k-nearest and nSigma of 5
- **White Points**: RGB mean > 48000 for white points
- **Black Points**: RGB mean < 4000 for black points
- **Sky**: ExB > 18000

Points which do not match with any formula remain unclassified and are possible sediment points. Finally, the remaining point cloud was exported as subset for sediment classification (Section 2.7).

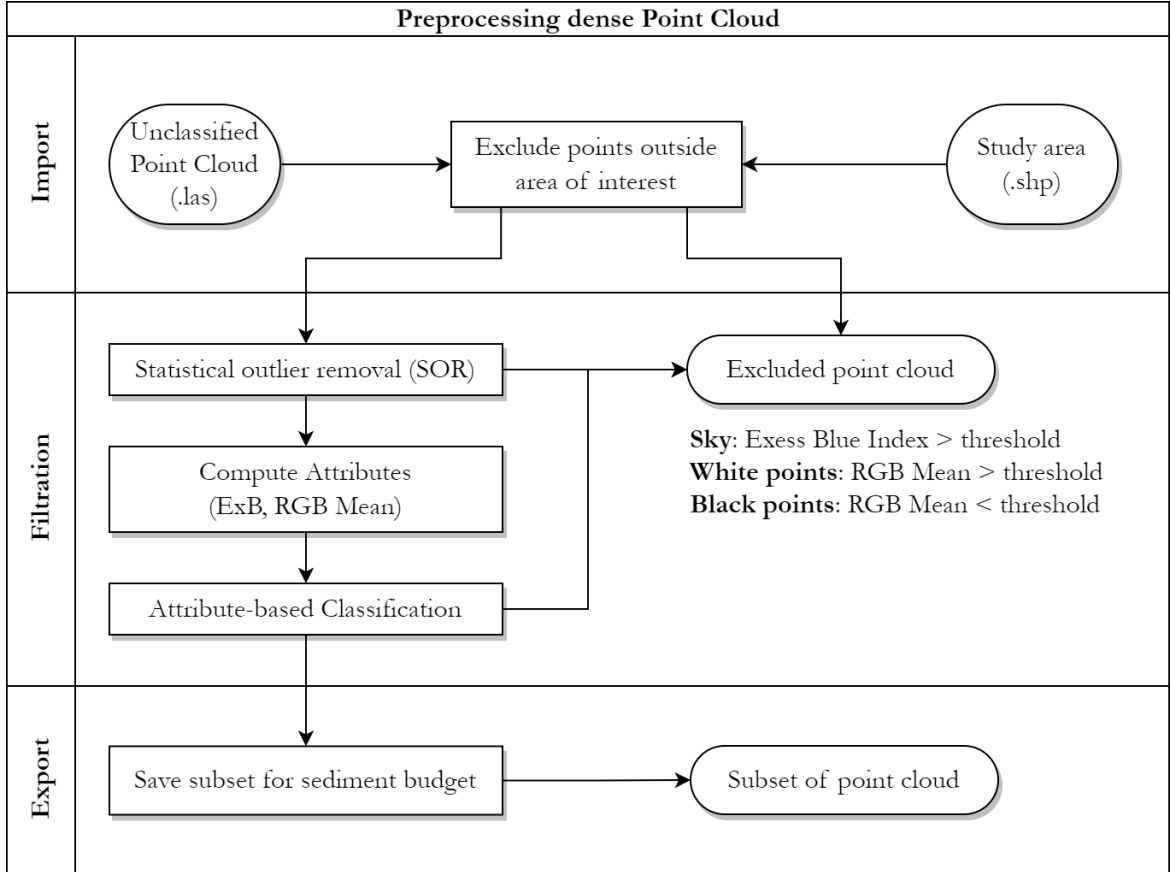


Figure 2: Schematic overview of the implemented pre-processing routine for dense point clouds. First, points outside the investigated area were excluded from the point cloud. Second, statistical outlier removal (SOR) was applied to filter mid-air points. Third, with RGB mean white and black points were filtered, with excess blue index (ExB) sky points were filtered. Finally, the remaining point cloud was exported as subset for sediment budgeting.

## 2.7 CSF classification routine

In a next step, a sediment classification of the filtered point cloud was examined based on CSF (W. Zhang et al., 2016). For UAV data, a prior classification of water surface was required before sediment points were classified. For this, CSF: (i) applies a rotation of the point cloud by a horizontal symmetry axis and then (ii) simulates a physical process which drops a rigid cloth on the rotated point cloud. With the interactions between cloth nodes

and the rotated surface, an approximation of the ground surface is generated as result. Based on this method, a routine was built (Figure 3) which identifies sediment points and, if apparent, distinguishes water points. The developed routine uses parameters `rigidness`, `cloth_resolution` and `class_threshold` (W. Zhang et al., 2016) as input for the command `classify_gnd()` implemented by Roussel & Qi (2018). The developed routine incorporates also a goodness-of-fit function (GOF) which compares the agreement of CSF output with a reference map using the well-established Cohen kappa ( $C_{kappa}$ , Antonetti et al., 2016; Cohen, 1960). For the comparison, intermediate results and reference data are rasterized with an identical `raster_resolution` and rated with  $C_{kappa}$ , which returns an agreement score between 0 (poor fit) and 1 (perfect fit). For point cloud with present water surface (UAV), the developed routine generated a binary water mask first to mask out water bodies from the generated sediment raster (Figure 3).

### 2.7.1 Parameter optimization

With the aim of finding an optimized parameter set, developed routine was then embedded in a genetic algorithm developed by Scrucca (2013). Such genetic algorithm are used as optimization method for finding ideal parameter sets of a complex multidimensional model (Berkemeier et al., 2017). For this, the genetic algorithm simulates the evolution of organisms with functions like selection, crossover and mutation (Scrucca, 2013). In this case, the returned agreement score represents the survived population of a living organism, which evolves over the four genes `cloth_resolution`, `class_threshold`, `rigidness` and `raster_resolution`. First, this complex issue was approached with a four dimensional parameter search for water bodies. Beforehand, trial runs were used to test the sensitivity of the input parameter `raster_resolution` at resolutions 0.2, 0.3 and 0.4 m. With `raster_resolution` set at 0.4 m, the highest fit for water bodies was searched. The best parameters of this search were then used as static input for the sediment parameter search.

## 2.8 Sediment Budget

With the obtained results from CSF classification, a sediment budget was calculated. For each point cloud, CSF parameters with the highest agreement were applied. This implicated the use of a raster resolution of 0.4 meter. Similar to Lane et al. (2003) and Brasington et al. (2003), the raster products were subtracted from each other, resulting DoD which shows the elevation change of sediment areas between time step  $t_0$  and  $t_1$ . Before an DoD could be applied, only raster cells which remained terrestrial sediment in time step  $t_0$  and  $t_1$  were selected. For this, a 2D habitat change analysis was performed beforehand showing changes of rasterized terrestrial sediment between  $t_0$  and  $t_1$ . For each raster cell, a habitat class was assigned, either: *New deposition*, if sediment was only abundant in  $t_1$ ; *New erosion*, if sediment showed abundance in  $t_0$  but did not appear in  $t_1$  and *Unchanged*, if no terrestrial sediment was present in both time steps (Table 4). Raster cells with present sediment in  $t_0$  and  $t_1$  were assigned to the class *Change in elevation* and taken into account for sediment budgeting, since this is the only class with a valid change in elevation.

Table 4: Assigned habitat classes for the 2D habitat change analysis based on rasterized terrestrial sediment areas of time steps  $t_0$  and  $t_1$ .

Sediment $t_0$	Sediment $t_1$	Habitat class
not present	not present	unchanged
not present	present	new deposition
present	not present	new erosion
present	present	change in elevation

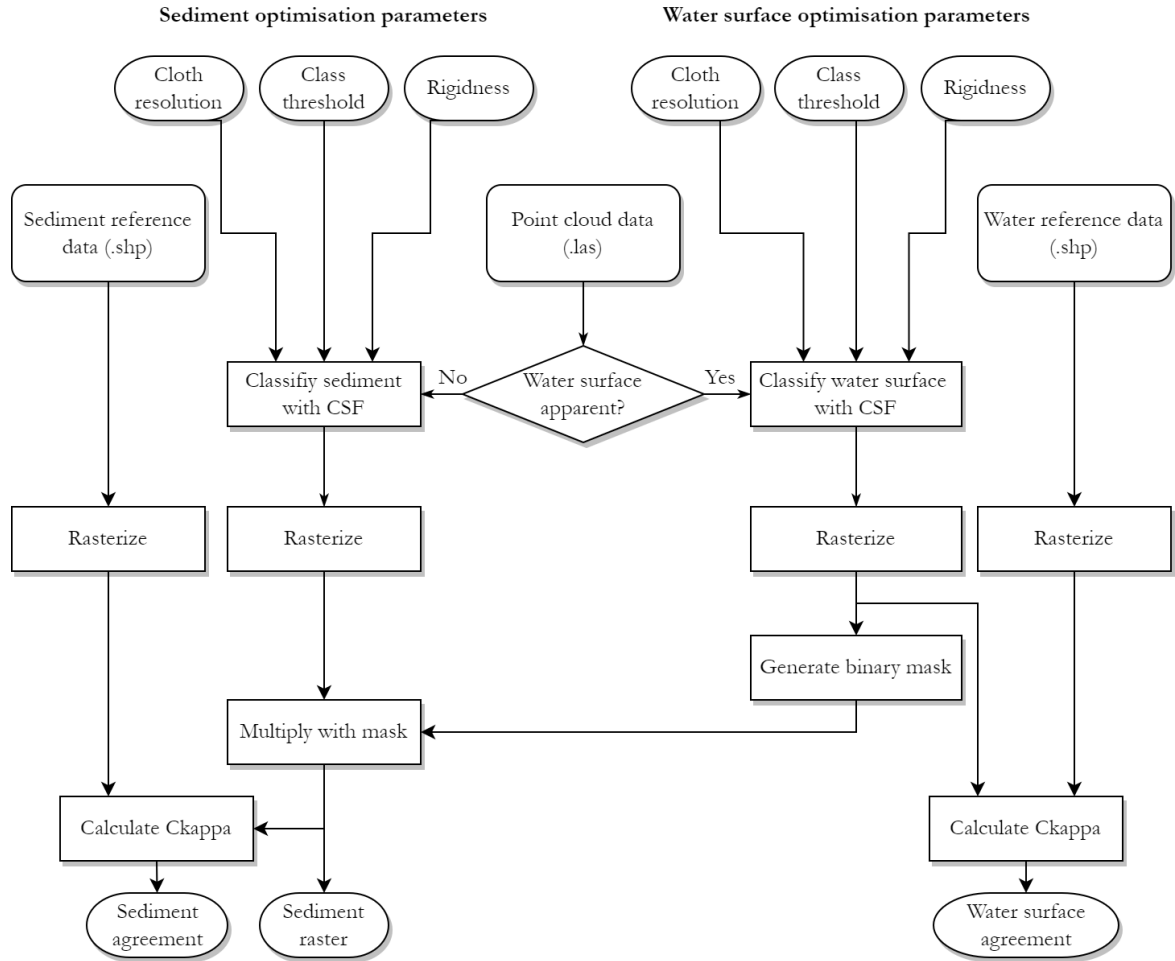


Figure 3: Schematic overview of developed CSF classification routine. First, the provided point cloud is classified with the function `classify_gnd()` based on the parameters `cloth_resolution`, `class_threshold` and `rigidness`. This is done with a different parameter set for each target body (water surface and sediment). Both intermediate results are rasterized with the same raster resolution. As raster, water surface is masked out by a binary mask from sediment classification. Based on a goodness-of-fit-function ( $C_{kappa}$ ), the function also compared the intermediate results with reference data and returned an agreement score.

The intermediate result was undertaken a probabilistic uncertainty assessment as proposed by Brasington et al. (2003) and Lane et al. (2003). The uncertainty of the DoD is accounted in three steps:

1. quantifying the surface representation uncertainty in the individual DEM
2. propagating the identified uncertainties into the DoD
3. assessing the significance of propagated uncertainty.

This workflow results in defining a critical level of detection ( $LoD_{crit}$ ) where elevation change cannot be distinguished from normal noise. Elevation changes below  $LoD_{crit}$  are discarded for the sediment budget which results in loss of information. With the assumption that errors in elevation are random, independent and show a Gaussian distribution,  $LoD_{crit}$  was calculated with:

$$LoD_{crit} = t \sqrt{\sigma_{t0}^2 + \sigma_{t1}^2}$$

where  $\sigma_{t0}$  and  $\sigma_{t1}$  are the standard deviation of error (SDE) in each data set.  $t$  represents the t value of a specific confidence level and was set at 1.96 ( $2\sigma$ ), which equals to 95 % confidence limit (Brasington et al., 2003; Brasington et al., 2000; Croke et al., 2013; Dai et al., 2022; Milan et al., 2007; Wheaton et al., 2009). The SDE of UAV data was derived from the computed Pix4D results. For the UAV data of 2022, an additional manual measurement of 17 validation targets was examined three times with an alternating order of GCPs and compared to the computed SDE. A manual measurement of the same targets was applied for the TLS data of 2022 in ArcGIS Pro. The obtained  $LoD_{crit}$  of each interval was then used to propagate these uncertainties into the calculated DoD and discard cells which are below the threshold. A comparison between the discarded area versus valid area allowed the significance of the calculated sediment budget to be assessed. Finally, cells above  $LoD_{crit}$  were used for the calculation of volumetric changes resulting in a sediment budget of terrestrial sediment volumes.

Additionally, two maps were derived from the developed routine: (i) an 2D habitat change map and (ii) an elevation change map, both indicating the spatio-morphological impact of the flood. As third additional result, each DoD was used to exhibit the elevation change distribution (ECD, Wheaton et al., 2009). Displayed as a histogram it was used to interpret the characteristic impact of each flood event and check the integrity of the developed routines and point cloud data.

With the acquisition methods used, this work focuses on terrestrial sediment areas of a riverbed only, submerged areas were ignored. Since the investigated area represents a residual flow section, low flow conditions and similar water surface levels are ensured by hydropower production. Vast parts of this routine are implemented with functions of the R packages **lidR** (Roussel et al., 2020), **raster** (Hijmans, Etten, et al., 2023), **terra** (Hijmans, Bivand, et al., 2023) and **sf** (Pebesma, 2018) which are dedicated packages for efficient processing of spatial data, especially large point cloud data. The packages **tmap** (Tennekes, 2018), **tidyverse** (Wickham et al., 2019) and **cowplot** (Wilke, 2020) were used for visualization and data processing of the results.

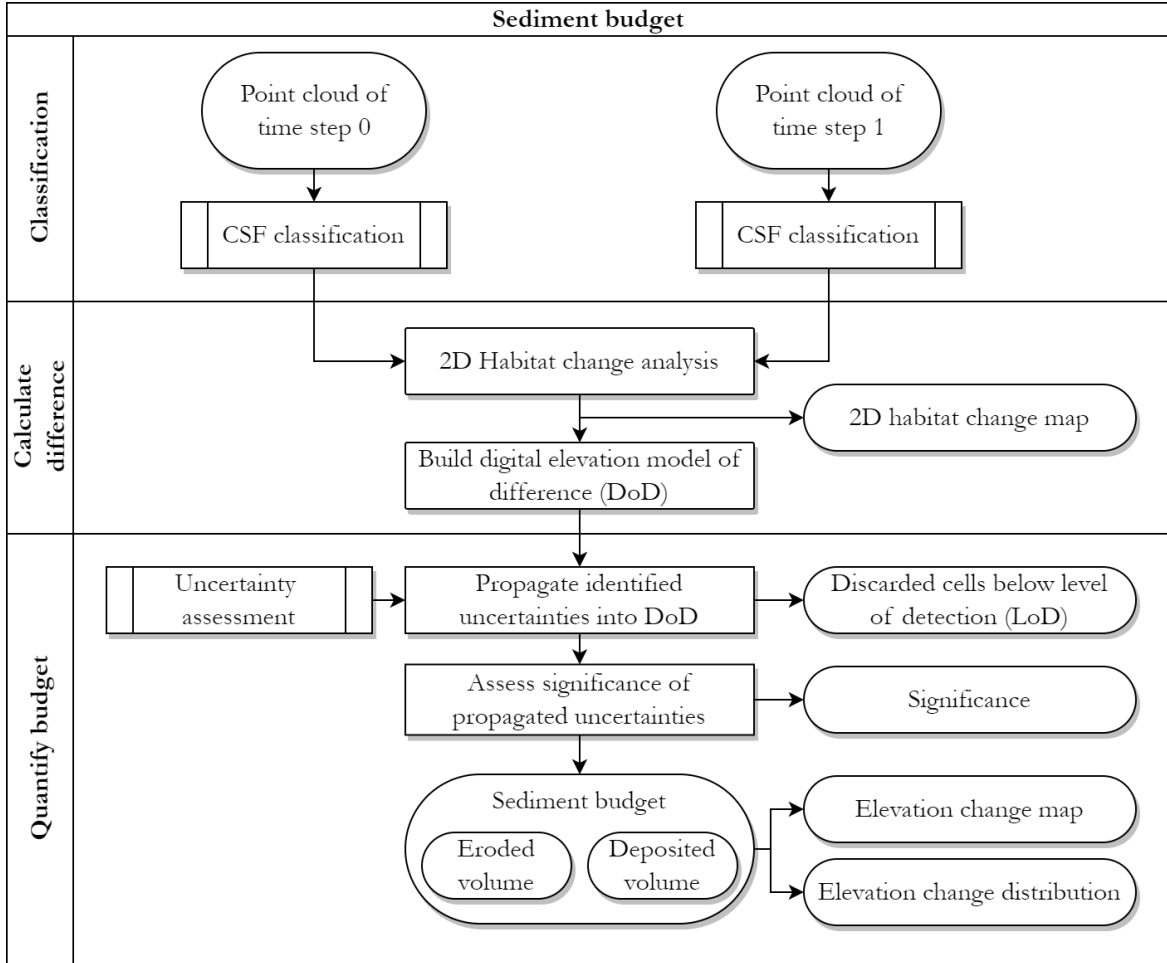


Figure 4: Schematic overview of the implemented sediment budget routine. First, with the CSF classification routine sediment points were retrieved for point cloud t0 and t1. Second, a 2D habitat change analysis was examined to obtain only valid elevation changes. Third, a digital elevation model of difference (DoD) was built and the assessed uncertainties were propagated into the DoD. Cells below the critical level of detection were discarded and the significance of the propagated uncertainties was assessed. Finally, a terrestrial sediment budget was obtained. The obtained results include a separate volume calculation of erosion and deposition, an elevation change map and an elevation change distribution (ECD).

### 3 Results

#### 3.1 Automated classification of sediment and water bodies

The automatically generated point clouds derived from the genetic algorithm (Scrucca, 2013) of the classes water surface and sediment show different agreements compared to their correspondent reference (Figure 5). All obtained scores of the class water surface show a substantial agreement ( $C_{kappa} > 0.6$ ) whereas obtained results of the class sediment show lower agreement. The obtained agreements of sediment classes vary between a fair ( $C_{kappa} > 0.2$ ) and moderate ( $C_{kappa} > 0.4$ ) agreement (Landis & Koch, 1977). The highest sediment agreement for UAV data was achieved with Wingtra One data (point density: 184 points/m<sup>2</sup>), whereas with eBee Plus data only 0.445 was achieved (point density: 32.21 points/m<sup>2</sup>). A similar  $C_{kappa}$  is achieved with TLS data from 2021 (0.547). Overall, TLS-based classifications does not achieve higher  $C_{kappa}$  than UAV-based classifications. Compared to sediment class agreements, the best water surface agreements only vary between 0.728 (5.11.20) and 0.792 (8.10.20) for all data sets. The CSF input parameter **rigidness** affects the agreement of TLS data, whereas UAV data is hardly affected (Figure 5). For water surface identification three out of four data sets show a similar pattern (Figure 6). Except the data set from 5.11.20, substantial  $C_{kappa}$  are achieved with **class\_threshold** between 0.1 and 2. It can be identified that this is also the most sensitive range of the parameter **class\_threshold**. From **class\_threshold** > 2  $C_{kappa}$  starts to decrease towards a local minimum around 3. After the local minimum agreements start to increase but do not reach best scores again. At **class\_threshold** = 6 and greater  $C_{kappa}$  decreases in a uniform and less sensitive manner over all data sets. The obtained results reveal that parameter **cloth\_resolution** is less sensitive when **class\_threshold** is greater than 4 (see Figure 6). Below this, **cloth\_resolution** shows a less uniform and distinct pattern than other CSF parameter, which leads to multiple local peaks in all data sets between 5 and 20. Over all tested data sets, these local peaks mainly gather at **cloth\_resolution** ~ 15 for water surface identification. Even though the parameter optimization for water surface showed a similar behavior over all data sets, no parameter set with global validity was found.

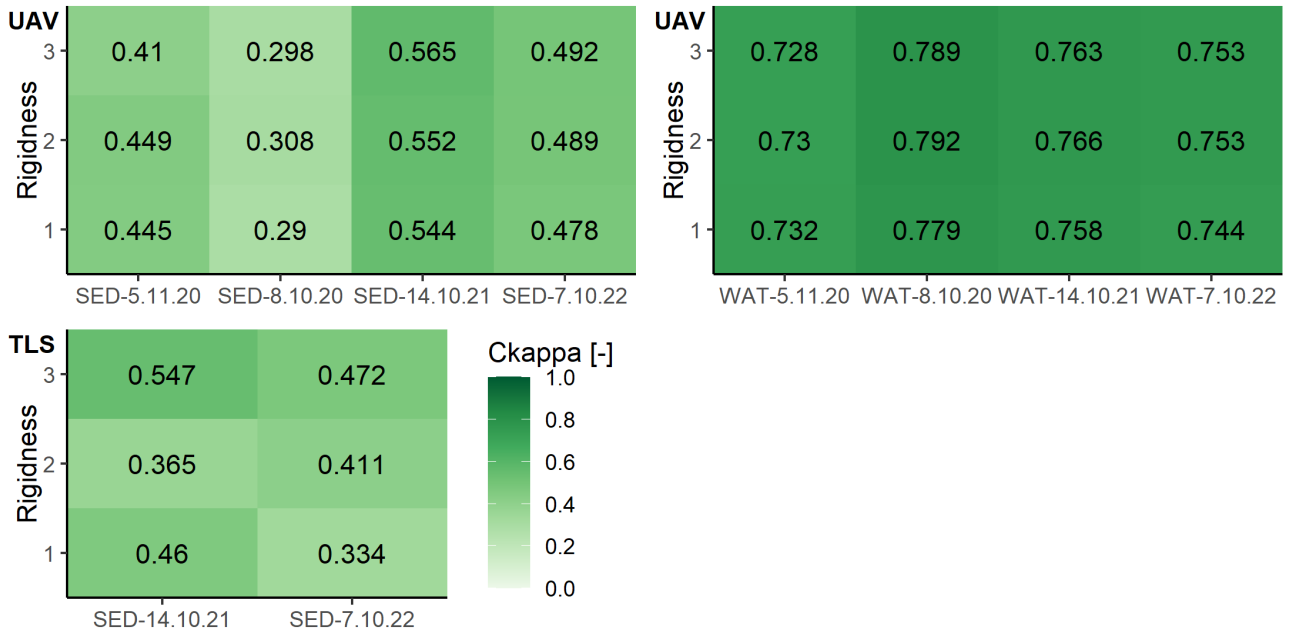


Figure 5: Highest agreement scores of  $C_{kappa}$  obtained by comparing the maps derived from Cloth Simulation Filter (CSF) with reference maps of the investigated area sorted by dataset and CSF parameter rigidness. For UAV data a raster resolution of 0.4 m was applied, whereas for TLS data 0.2 m was applied. Targeted bodies are abbreviated with SED = Sediment and WAT = Water.

A similar pattern is observed for sediment identification (Figure 7). For the UAV data, the genetic algorithm did find a distinct local minimum at `class_threshold`  $\sim 4$ , none of the best agreements of each data set was achieved with `class_threshold`  $> 4$ . Different to water surface identification, the CSF performed best results at the lower end of the tested range (`class_threshold`  $\sim 0.2$ ). Compared to water surface identification, `cloth_resolution` shows a more distinct pattern below `class_threshold` = 4. Best fits with the reference data are achieved with `cloth_resolution`  $\sim 3$ , independent of dataset or `rigidness`. Furthermore, the results reveal higher agreements for the data sets of 2021 and 2022, which were acquired with the Wingtra One. This observation does not align with the results from water surface identification, where the eBee Plus data from 8.10.20 delivered the highest agreement score over all data sets (Figure 5).

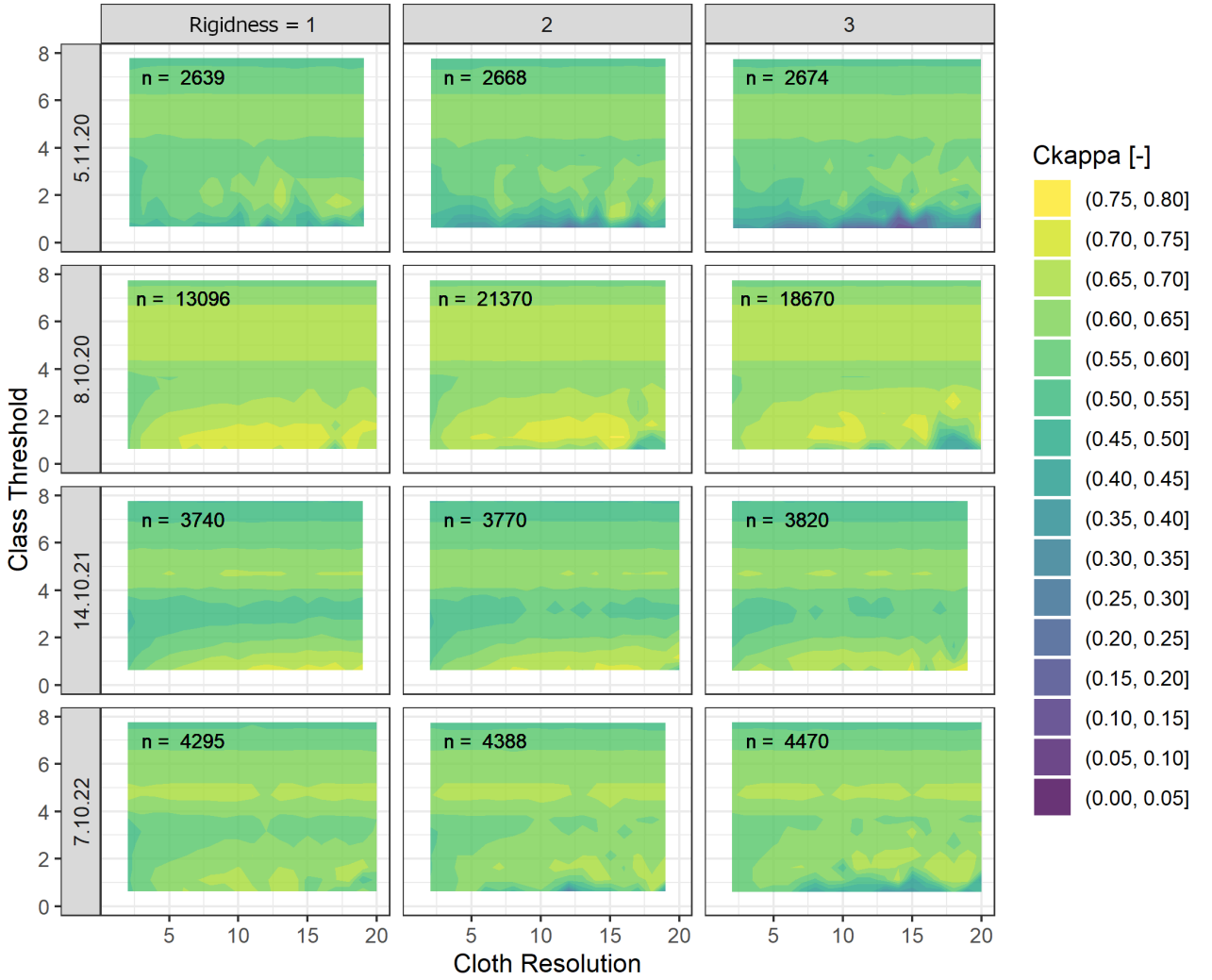


Figure 6: Distribution of agreement ( $C_{kappa}$ ) for water surface bodies after CSF classification was applied on UAV point clouds and compared to a reference. Every row corresponds to a data set, whereas each column represents a different rigidness value. Each subplot shows a heat map of  $C_{kappa}$  obtained varying class threshold (y axis) and cloth resolution (x axis). The parameter search was applied with a raster resolution of 0.4 m (n = number of observations).

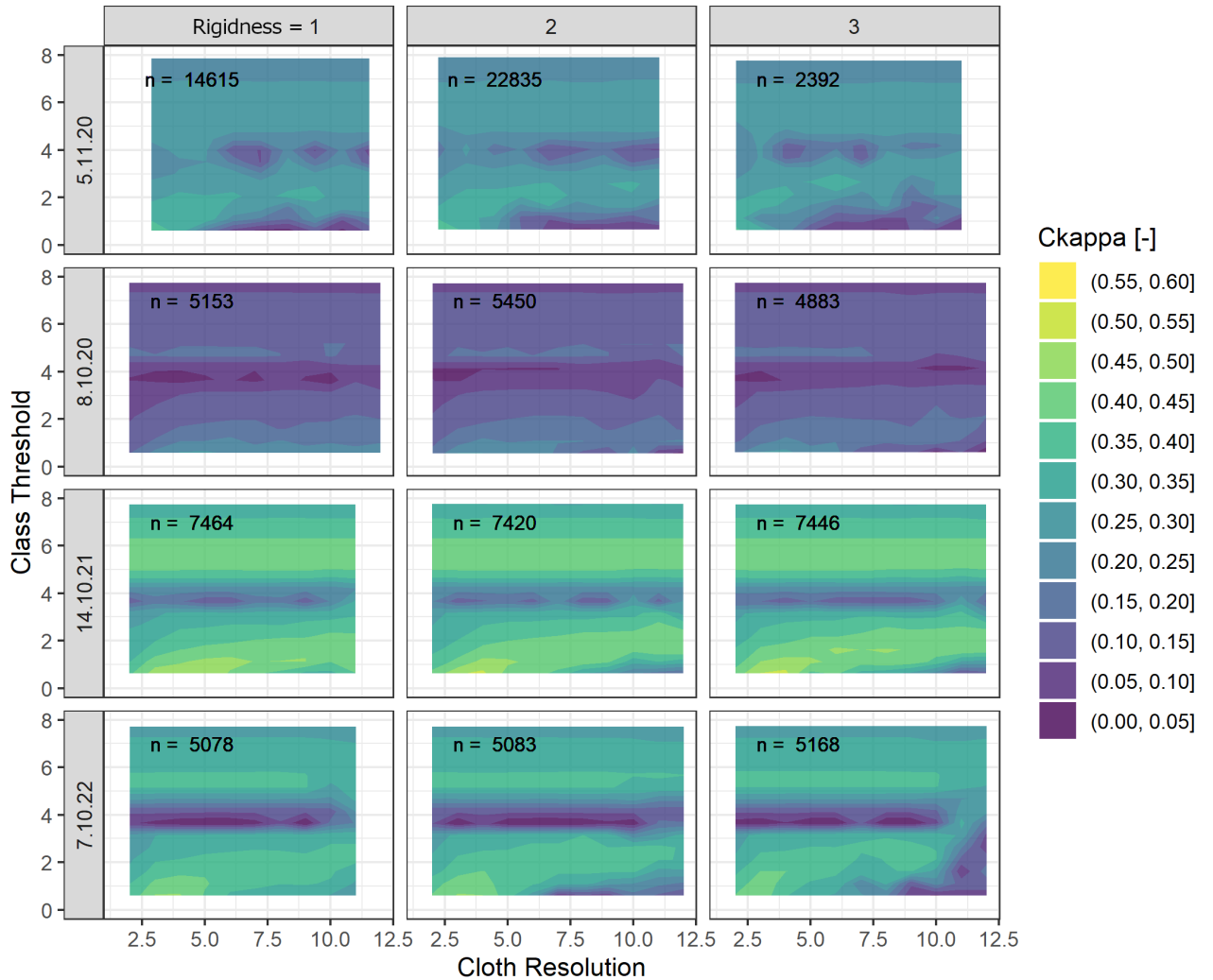


Figure 7: Distribution of agreement ( $C_{kappa}$ ) for sediment bodies after CSF classification was applied on UAV point clouds and compared to a reference. Every row corresponds to a data set, whereas each column represents a different rigidness value. Each subplot shows a heat map of  $C_{kappa}$  obtained varying class threshold (y axis) and cloth resolution (x axis). The parameter search was applied with a raster resolution of 0.4 m (n = number of observations).

### 3.2 Added value of sediment budgets derived from TLS data

A variation of the input parameter `raster_resolution` between 0.2, 0.3 and 0.4 m reveals that the correspondent agreement scores derived from TLS and UAV data differ (Figure 8). The comparison of the sixty best  $C_{kappa}$  of each test reveal a divergent tendency between TLS and UAV data.  $C_{kappa}$  of TLS data tend to span over a smaller interval, but deliver some of the best result as outlier. Conversely, UAV data show wider but more uniform intervals which tend to narrow towards higher resolutions. Data acquired from a terrestrial perspective achieves the best scores with the highest tested resolution (0.2 m), always showing a higher maximum agreement than the lower resolution. For UAV data the contrary trend is less obvious, showing an increasing median score with decreasing resolution but also delivering stable maximum scores around 0.49 over all tested resolutions for the 2022 data set (Figure 8). For further results, therefore, a resolution of 0.2 m for TLS data and 0.4 m for UAV data is chosen.

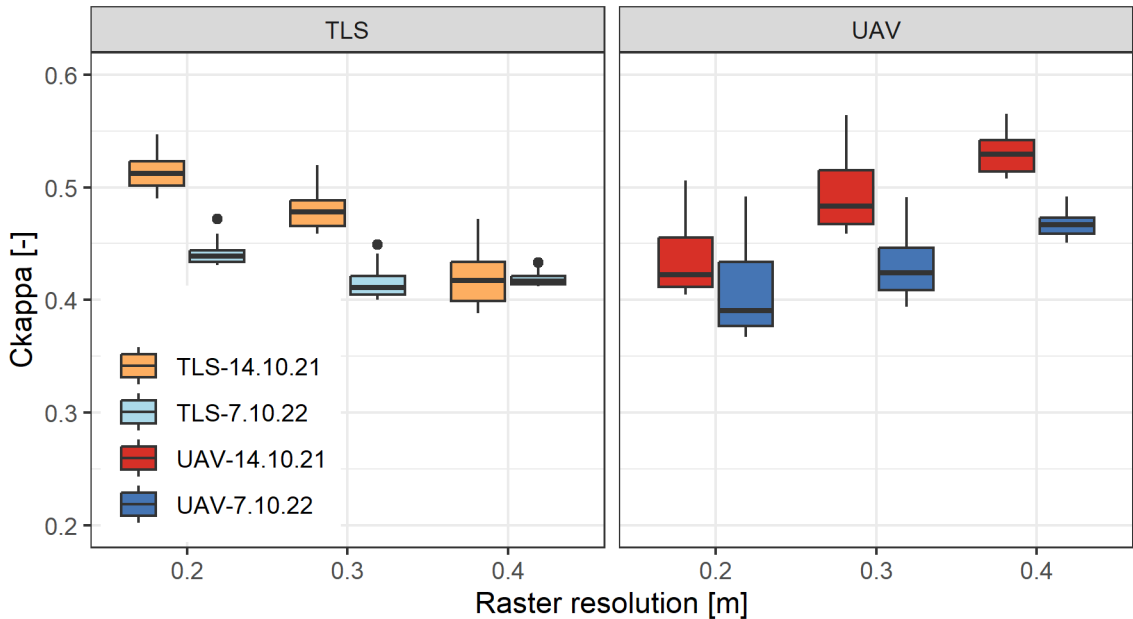


Figure 8: A comparison of TLS (left) and UAV (right) sediment agreement scores ( $C_{kappa}$ ) derived from CSF classification when compared with reference data and altered input parameter raster resolution (tested at 0.2, 0.3 and 0.4 m).

The sediment bar at the lower end of the investigated area was correctly identified by both UAV and TLS data (A on Figure 9). The sediment banks of the island were also correctly identified by UAV-based classifications to a broad extent, whereas TLS-based classifications only identified minor patches of this area (B on Figure 9). UAV-based classifications seem to match sediment areas clearly better, although both TLS-based classifications achieved similar  $C_{kappa}$  for sediment within its correspondent investigated area (0.547 and 0.472 for TLS, 0.565 and 0.492 for UAV). TLS-based classifications identified sediment not visible from the UAV perspective located on the banks of the main channel along the island, although these areas were not included in the reference data (C on Figure 9). This observation shows that UAV-based classifications missed sediment areas where overhanging vegetation obstructed the view.

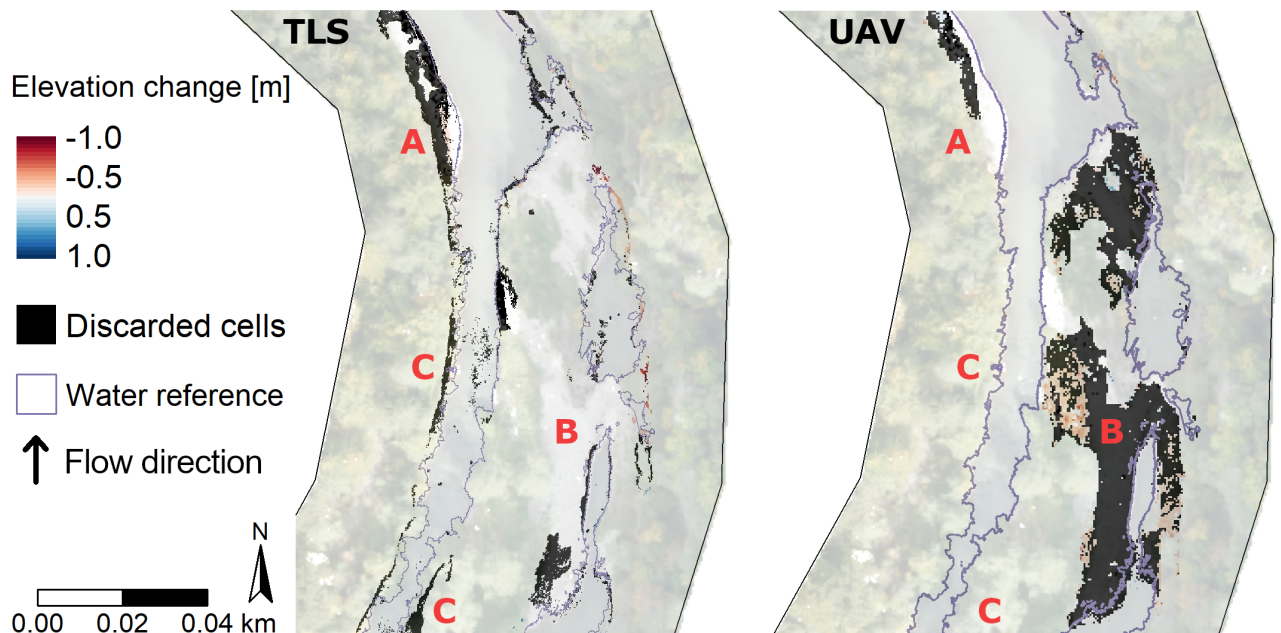


Figure 9: Digital elevation model of difference (DoD) obtained from the artificial flood on the 31.05.2022, showing best results of TLS (left) and UAV (right) and water reference in violet. For TLS, critical level of detection (LoD) was set at 0.18 m, raster resolution at 0.2 m. For UAV, LoD was thresholded at 0.15 m, raster resolution at 0.4 m. After the application of LoD, discarded cells are shown in black, erosion in red and deposition in blue. The CSF classification of UAV and TLS data impacted the DoD differently, showing different classification results of a sediment bank (A), the main island (B) and below vegetation (C). (Source: Orthoimage after the flood event on the 7.10.2022 by the Ecohydrology research group).

### 3.3 Impact of flood events 2020, 2021 and 2022 on terrestrial sediment volumes

#### 3.3.1 Spatiotemporal distribution of terrestrial sediment habitats

Gain and loss of eroded and deposited areas vary between the different floods (Figure 10). On a qualitative level, the flood of 2020 mainly caused new deposition of sediment within the investigated area (Figure 10a). Deposition is evident at the head of the lower side channel (C on Figure 10a) and along active side-channel of the island (B on Figure 10a). Only, small patches of erosion are observed and two sediment banks are missed by CSF classification (D and E on Figure 10a). This artificial flood is followed by a longer natural flood event in 2021 which eroded parts of the sediments deposited in 2020 (Figure 10b). At the inner reach of the meander (B on Figure 10b), a rearrangement of sediment areas is observed, building patches of all classes which vary in size and frequency. Besides deposition at the beginning of the investigated area (A on Figure 10b) and along shores, sediment banks are created in the lower area (C on Figure 10b), whereas one bank is missed on the resulting map (D on Figure 10b). These sediment banks are eroded with the following flood in 2022 (Figure 10c). Distributed over the entire area, more erosion is present, with a focus on the upper side-channel (A Figure 10c), the head of the island (B on Figure 10c) and the lower end of the investigated area (E Figure 10c). One sediment bank is missed by the CSF classification (D on Figure 10c).

#### 3.3.2 Estimation of surface representation uncertainty

As proposed, the surface representation uncertainty is estimated to define  $LoD_{crit}$  (Figure 11). For the UAV data of 2022, the manually measured standard deviation of error in z direction ( $SDE_z$ ) yields 0.063, 0.045 and 0.053 m resulting in an average of 0.0536 m. For the TLS data of the same year, only 8 validation targets could be used for the measurement due to coverage caused by vegetation and rocks hindered the use of further validation targets (details in appendix C and F). These targets yielded a  $SDE_z$  of 0.063 m (Figure 11 b). Since no validation targets are apparent for prior flights the  $SDE_z$  of validation targets have been used for  $t_0$  and  $t_1$  which results in  $LoD_{crit}$  of 0.1737 m for TLS data and 0.1486 m for UAV data (Figure 11 c). For sediment budgeting based on UAV data with no available validation targets (eBee Plus flights) the SDE of the SfM process in z direction is used as comparison, revealing an SDE of 0.0194 m and 0.0345 m for the eBee Plus, 0.0122 and 0.0192 m for the Wingtra One (Figure 11 a). Since  $SDE_z$  of SfM processing is lower than  $SDE_z$  measured by validation targets this leads to lower  $LoD_{crit}$  of 0.0776 m and 0.0774 m. Moreover, the Wingtra One flights were performed with a higher GCP density than flights performed with the eBee Plus. This leads to an underestimation of  $LoD_{crit}$  for data acquired by the eBee Plus. Therefore, a more conservative  $LoD_{crit}$  of 0.15 m is chosen and applied on all UAV data sets. Due to the fact that  $SDE_z$  of TLS data lead to a higher  $LoD_{crit}$  than the UAV data, only sediment budget results based on UAV data are highlighted in the following sections. Sediment budgets based on TLS data can be found in appendix H (with  $LoD_{crit} = 0.18m$ ).

#### 3.3.3 Calculation of sediment budgets

Compared to the 2D analysis, the sediment budget analysis shows a similar impact of each flood and reveals plausible geomorphic signatures (Table 5, Figure 12 and Figure 13). All analyzed floods exhibit an ECD with a kurtosis of elevation changes which differ in amplitude, skewness and center of the main peak.

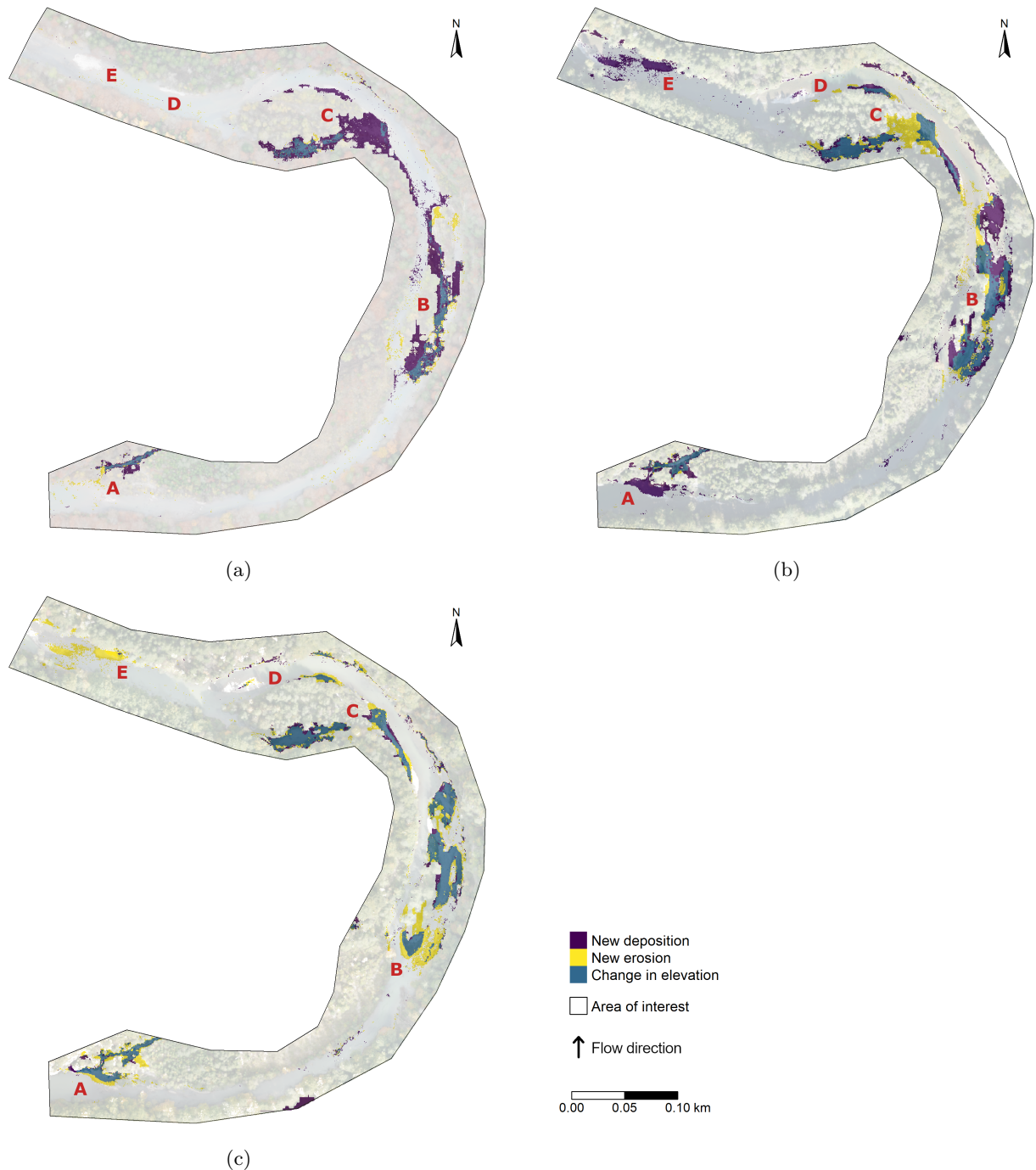


Figure 10: Overview of two-dimensional habitat change of terrestrial sediment areas derived from UAV data, showing impact of the floods in 2020 (a), 2021 (b) and 2022 (c). The map is divided into three classes: (i) new deposition, if habitat changed from water to sediment, (ii) new erosion, if habitat changed from sediment to water (iii) change in elevation, if sediment remained sediment (Source: Orthoimages after the flood events on the 8.10.2020 (a), 14.10.2021 (b), 7.10.2022 (c) provided by the Ecohydrology research group).

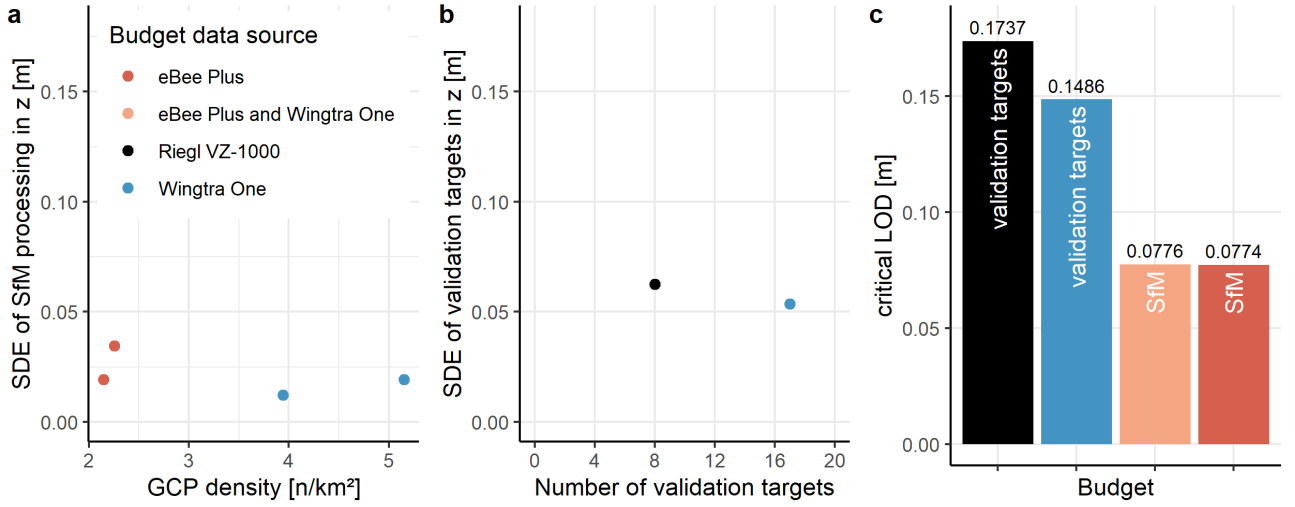


Figure 11: Estimation of surface representation uncertainty which consists of: (a) standard deviation of error (SDE) distribution in z direction derived from SfM processing in relation with the GCP density, (b) a distribution of the measured SDE for all available validation targets in relation with number of used GCPs, (c) the calculated critical level of detection (LoD) based on the stated SDE.

Table 5: Quantified terrestrial volumes derived from the DoD for each flood event, showing quantified deposited and eroded volumes separated by total and valid classes, (based upon the defined critical Level of detection), the percentage of discarded volumes and calculated zone average (only valid cells taken into calculation).

Flood date	Deposited volume			Eroded volume				
	Valid	Total	Discarded	Zone Average	Valid	Total	Discarded	Zone Average
22.10.20	11.4	17.7	35.62	0.272	-249.8	-272.6	8.37	-0.291
11.07.21	533.7	586.7	9.05	0.321	-136.7	-168.5	18.90	-0.330
31.05.22	29.4	71.4	58.83	0.284	-192.0	-347.1	44.69	-0.266
Unit	[m³]	[m³]	[%]	[m³/m²]	[m³]	[m³]	[%]	[m³/m²]

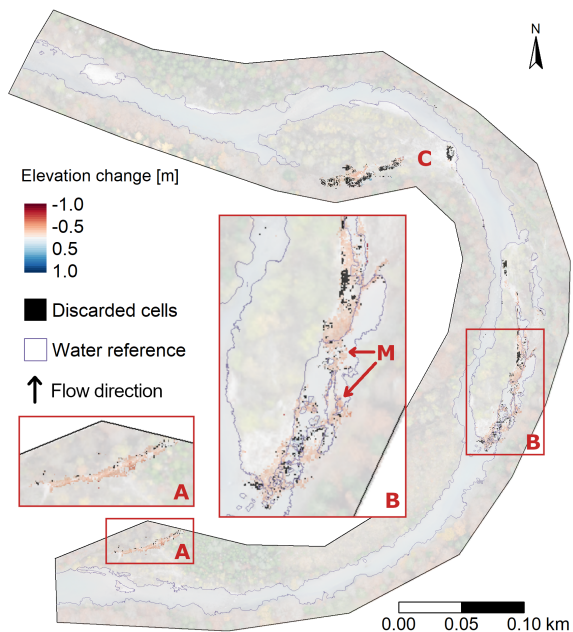
Within the investigated area, the flood in 2020 mainly led to erosion of sediment (Table 5). In total, 272.6 m<sup>3</sup> of terrestrial sediment were eroded, of which 249.8 m<sup>3</sup> are accounted as valid (91.63 % valid). This erosion can be located at the beginning of upper inactive channel, on the right side of the island and at the lower inactive channel (A, B and C on Figure 12a). Only minor patches of deposition are identified with a focus on the inactive side channel downstream and the island (B and C on Figure 12a), leading to a total deposition of 17.7 m<sup>3</sup> of which 35.62 % were discarded (Table 5). A detailed comparison of water surface reference with the computed DoD reveals that a small number of water raster cells are accounted into the budget (M on Figure 12a). These misclassified raster cells at the active side channel of the island lead to a minor overestimation of total eroded volumes. The stated volume changes are also represented as single-peak histogram with a blunt peak at -0.25 m in the correspondent ECD (Figure 12b), showing the erosional character of this flood. This is supported by the fact that 0.272 m<sup>3</sup>/m<sup>2</sup> is the lowest depositional zone average is reported among the analyzed floods.

With the natural flood event in 2021, the greatest rearrangement of terrestrial sediment volumes are reported. The almost 9-day lasting flood period caused deposition of 586.7 m<sup>3</sup> of which only 9.05 % were discarded. This deposition is spread over the upper two thirds of the investigated area with a focus at the active side channel of the island (B on Figure 12c). A total volume of 168.5 m<sup>3</sup> eroded terrestrial volume is accounted of which

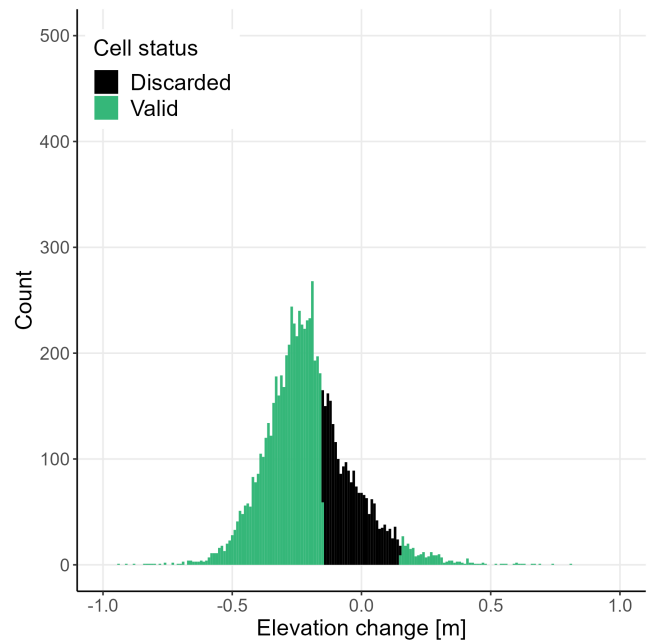
136.7 m<sup>3</sup> are accounted as valid (Table 5), mainly gathered at the center of the island and at the inactive side channel downstream (B and C on Figure 12c). A comparison with the water surface reference shows that a fair number of misclassified raster cells are located on the inactive side channel of the island (M on Figure 12c). The magnitude of this flood event is pointed out with the correspondent ECD (Figure 12d), revealing a histogram with two peaks: (i) a minor peak centered close to zero which is overlapped by (ii) a major peak at +0.3 m resulting in negatively skewed kurtosis with a steep gradient at the right side. Since misclassified raster cells are solely of depositional type, it leads to an overestimation of the major peak in Figure 12d. Additionally, the impact is also indicated in Table 5 showing the highest values of valid zone average over all analyzed floods, for both deposition (0.321 m<sup>3</sup>/m<sup>2</sup>) and erosion (-0.330 m<sup>3</sup>/m<sup>2</sup>).

Like the prior flood events, the latter flood event in 2022 shows an unique geomorphic signature indicated by the ECD in Figure 13b. Contrary to the other floods, this event caused a joint and uniformly skewed histogram with a single peak at -0.1 m. A closer comparison of water reference with the classified raster cells (Figure 13a) show that only a minor number of cells are misclassified, all below than  $LoD_{crit}$ . This even distribution close to zero leads to a major proportion of discarded terrestrial sediment volumes (58.83 % for deposition, 44.69 % for erosion) showing a slight tendency towards erosion. The shift of the single peak ECD towards erosion is also shown in accounted valid volumes with 29.4 m<sup>3</sup> terrestrial deposition and 192.0 m<sup>3</sup> terrestrial erosion (Table 5). The volumes are distributed over the investigated area with a focus at: (i) a patch at the head of the upper side channel, (ii) three major patches within the island, (iii) a sediment bank after the island and (iv) a major patch at the lower inactive side channel (A, B and C on Figure 13a).

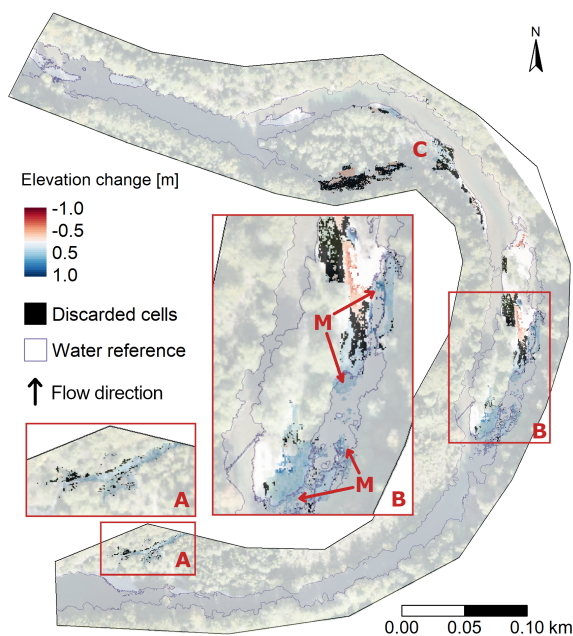
Overall, the analyzed floods can be compared in regard with maximum discharge and duration during the flood events in Figure 14. This figure suggests that the two minor flood events of 2020 and 2022 coined the investigated area mainly by erosion, whereas the greatest analyzed flood event (with maximum discharge of 302.3 m<sup>3</sup>/s and a duration of 212 h) had a distinct depositional impact on terrestrial sediment volumes. Apart from this single peak, the investigated area point towards an equilibrium with a slight erosional tendency. When all flood events are summarized, a total valid erosion of -578.4 m<sup>3</sup> (-788.2 m<sup>3</sup> including discarded volumes) versus a valid deposition of 574.5 m<sup>3</sup> (675.9 m<sup>3</sup>) is observed, resulting in a ratio of 1.007 of the quantified sediment volumes have been rearranged (1.166 including discarded volumes). Figure 14 B and C show a comparison of the assessed volumes in relation to the hydrological parameters of each event. The comparison indicates that the investigated area was shaped predominantly with erosion when the flood was of a minor magnitude (2020 and 2022), whereas deposition was predominant in the major flood in 2021.



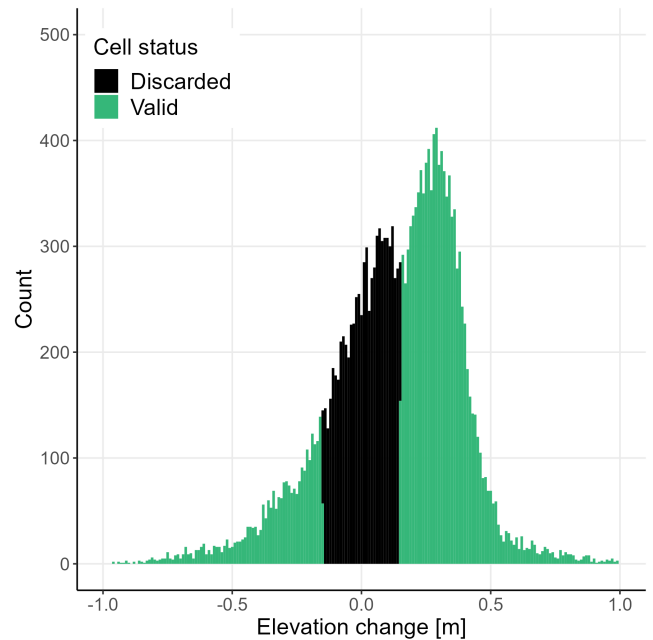
(a) DoD of the flood on 22.10.20



(b) ECD of the flood on 22.10.20



(c) DoD of the flood on 11.7.21



(d) ECD of the flood on 11.7.21

Figure 12: Derived sediment budgets from the floods on 22.10.20 (a and b) and 11.7.21 (c and d), showing a elevation change map and elevation change distribution (ECD) for each flood. Erosional elevation change is displayed in red, depositional in blue, elevation change below the critical level of detection (0.15 m) is displayed in black. Areas with pronounced sediment change are marked with A, B and C, misclassified areas with M. (Source: Orthoimages after the flood events on the 8.10.2020 and 14.10.2021 provided by the Ecohydrology research group).

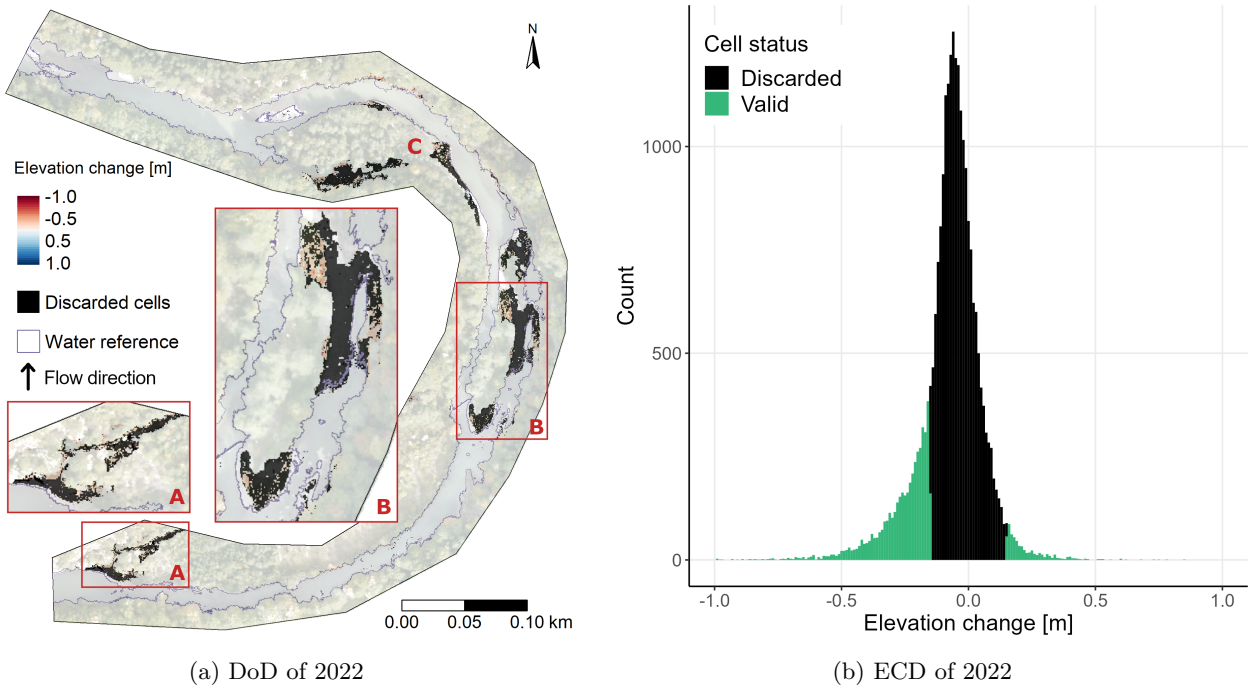


Figure 13: Derived sediment budgets from the flood on the 31.5.2022, showing a elevation change map and elevation change distribution (ECD). Erosional elevation change is displayed in red, depositional in blue, elevation change below the critical level of detection ( $0.15\text{ m}$ ) is displayed in black. Areas with pronounced sediment change are marked with A, B and C. (Source: Orthoimages after the flood events on the 7.10.2022 provided by the Ecohydrology research group).

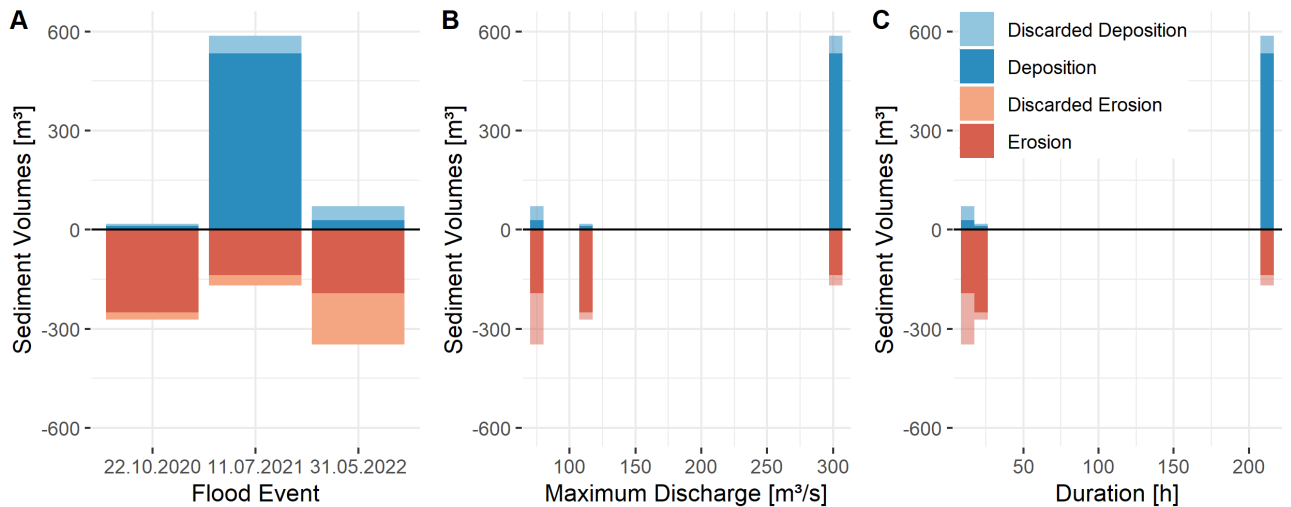


Figure 14: Comparison of the effects on terrestrial sediment volumes in regard with discharged volume and maximum discharge.

## 4 Discussion

### 4.1 Automated classification of sediment and water bodies

The results from the CSF classification routine showed that cloth simulation (W. Zhang et al., 2016) is suited for an automated classification of water surface and terrestrial sediment areas. Particularly for the classification of water surface, CSF is a robust method and capable of achieving substantial results. The investigated parameters `class_threshold`, `cloth_resolution` and `rigidness` showed a systematic pattern over all tested datasets. With a water surface agreement of  $C_{kappa} > 0.72$  over all data sets the herein presented agreements were in range with results retrieved from an artificial neural network (Casado et al., 2015) or indices-based classification (Sivanpillai & Miller, 2010) but lower than classification approaches based on intensity signal (Höfle et al., 2009; Morsy, 2017), point density (Lang & McCarty, 2009) or multi-spectral indices (Morsy et al., 2016).

In contrast to the substantial agreement scores retrieved for water surface, limitations became apparent for sediment classification. Only fair to moderate agreements were obtained for TLS and UAV data, whereas Casado et al. (2015) showed that higher agreements for sediment classes are possible. Multiple factors influenced the CSF classification and led to less constant and lower agreement scores. First, the analysis demonstrated a distinct difference between UAV data source and therefore point density. Agreement scores were generally higher ( $0.57 > C_{kappa} > 0.47$ ) with Wingtra One data, whereas eBee Plus data, with point densities almost six times lower than Wingtra One data, achieved only  $0.45 > C_{kappa} > 0.29$ . This restricted data quality seems to be no issue for the classification of wide and almost planar surfaces such as water but is less reliant when complex sediment structures are targeted. Second, the developed routine shows difficulties when multiple small fragments are targeted. This explanation is supported by weakest result (5.11.2020 with  $C_{kappa} < 0.31$ ) where reference data contains a few small patches of terrestrial sediment (see appendix E for comparison). Third, it seems that the developed routine is strong in distinguishing overhanging vegetation from almost planar water surfaces but weaker in distinguishing sediment areas from lower vegetation since, in some cases, this can be distinguished only by RGB information. Therefore, in cases where point metrics of neighboring features are similar and no additional signal is provided (e.g. intensity or infra-red signal), RGB approaches provide more promising results for UAV data (Casado et al., 2015; Scheib, 2022). Furthermore, the genetic algorithm used for CSF parameter optimization showed limited suitability for this optimization problem and lead to the limitation of only three dimensional optimization. Additional fine tuning of the used algorithm would be required to allow a more dimensional optimization. However, it became evident that under certain circumstances (high point density, low fragmentation) CSF delivers satisfactory results for terrestrial sediment classification derived from UAV data.

Classification results derived from TLS data showed similar agreements compared to UAV data. Different to UAV data,  $C_{kappa}$  derived from TLS data spanned over a smaller range but delivered some of the best result as outlier (see Figure 8). This less distinct behavior may be influenced by multiple factors. First, restricted search conditions, as due to rapid increase of computational time when `class_threshold` < 0.1, the lower boundary was set there. This boundary might have affected results negatively, since Bailey et al. (2022) showed that TLS data with similar point densities achieved best results at `class_threshold` = 0.009. Second, a bias was introduced since the provided reference data were based on UAV data, tested data sets of the same type were privileged. Although sediment areas below overhanging vegetation were indicated in the TLS data (Figure 9) it impacted  $C_{kappa}$  negatively. Third, Bailey et al. (2022) achieved best results with `time_step` = 0.15, a parameter which remained at its default value (0.65) in this work. However, whether investigations of a planar hillslope (Bailey et al., 2022) can be transferred to a complex and densely vegetated floodplain remains an open question. It also remains unclear whether CSF delivers satisfactory results for TLS data, since higher agreements might be achieved when parameter search is continued with an edited parameter set. However, the moderate CSF classification results propagated into the DoD and lead to a sediment budget linked with high uncertainties.

## 4.2 TLS for complex and densely vegetated floodplains

For the second research question, it could be demonstrated that TLS data provides added value when used for sediment budgeting in complex and densely vegetated floodplains on reach scale. Where overhanging vegetation partially obscures the sight of underlying terrestrial sediment areas for UAV data, TLS data adds value (Figure 9). Additionally and in alignment with Brasington et al. (2012), geomorphological changes along river sections can be exhibited with higher resolution. An increasing agreement score was observed for a decreasing raster resolution indicating the higher quality of TLS data (Figure 8). Another added value was provided by the experimental design: due to none water-penetrating laser, no water surface classification was required. It clearly shortened the workflow for this work but can be limiting for sediment budgets with different focus. For more holistic data acquisition and sediment budget estimation, the combination with a water-penetrating laser (Mandlburger et al., 2015) is crucial. However and apart from the stated advantages, limitations of TLS data became evident as well. First and foremost, the CSF results based on TLS data directly impacted the workflow in a pronounced manner (discussed in Section 4.1) leading to a sediment budget which, compared to the UAV results, lacks in quality.

### 4.2.1 Accurate TLS surface representation remains a challenge

With a measured  $SDE_z$  of 0.06267 m, no added value respective surface representation uncertainty could be observed for TLS data. Although the measured  $SDE_z$  is in alignment with measurements obtained by Brasington et al. (2012) it does not reach elevation errors < 0.01 m measured by Hodge et al. (2009). Consequently, the propagated  $LoD_{crit}$  was higher as Milan et al. (2007) presented (0.02 m). The uncertainty range found is reasonable but was expected to be lower than the  $SDE_z$  obtained from UAV data (0.0536 m). This observation suggests that, either different systematic errors were introduced or multi-resolution assessments are necessary to achieve higher accuracies (Brasington et al., 2012). For this work, it is unlikely that multi-resolution assessments had lead to a smaller SDE, since planar GCP surfaces were used as validation target. It is more likely that multiple erroneous effects lead to this uncertainty. First, the used RTK-GPS contributes up to 0.05 m to the elevation uncertainty (Trimble Incorporated, 2021). Second, the manual georeferencing procedure (multi-station adjustment and reprojection) of TLS point clouds with reference spheres might have caused an systematic error. Third, some validation targets of TLS point cloud showed poor to fair visibility (see appendix C and F). All these uncertainty sources made an accurate measurement challenging and, according to Gindraux et al. (2017), increased elevation error. Finally, environmental effects might have been introduced georeferencing errors, since GCPs remained distributed for a five day period (between TLS and UAV measurement). This assumption is supported by the evidence that UAV data, which was acquired on the same day as the RTK-GPS measurement, shows a lower  $SDE_z$  than TLS data.

## 4.3 Sediment budgets derived from UAV-SfM point clouds

### 4.3.1 Quantitative effects of the floods 2020, 2021 and 2022

The quantified volumes showed that floods of minor magnitude and duration revealed an erosional impact on the investigated area, whereas the major flood had an depositional impact. The magnitude of this major flood event ( $Q_{max} = 302.3 \text{ m}^3/\text{s}$ ) caused a mobilization sediment further upstream and led to the pronounced deposition of terrestrial sediment in 2021. This is supported by former research: during an artificial flood in 2016 at the Sarine, Döring et al. (2018) observed that coarser sediment was mobilized at a discharge of 140-175  $\text{m}^3/\text{s}$ . Additionally, findings from an ecohydrological simulation concluded that a discharge of at least 240  $\text{m}^3/\text{s}$  would lead to the mobilization of medium sized grains in the main channel Flükiger (2022). Therefore, the provided facts indicate that the sediment budgets are a plausible geomorphological response to the hydrological conditions of the flood (magnitude and duration). This conclusion is in alignment with findings of Döring et al. (2018) and Tonolla et al. (2021), who observed a sediment deficit along the same residual flow section.

A more detailed interpretation reveals the different impacts of each flood event. In 2020, the highest amount of valid erosion volumes was observed, accomplished by a small amount of deposited volumes. The DoD (Figure 12a) showed a small number of misclassified raster cells, which led to an overestimation of eroded volumes. Even

without taking this into account, the estimated impact of this flood is smaller than that one of the flood in 2022, which was of smaller magnitude and duration. In 2021, the majority of the sediment was deposited at the active side channel of the island. A more detailed analysis of the DoD shows a fair amount of misclassified volumes (Figure 12c) which points towards an overestimation of deposited sediment. Nonetheless, the distinct depositional character of the flood remains (Figure 12d). The latter analyzed flood impacted the investigated area in an almost uniform way with a tendency towards erosion. A near to symmetrical ECD (Figure 13b), combined with its minor magnitude and duration, resulted in the greatest amount of discarded volumes, although the rearranged sediment areas were widespread. The flood occurred in 2022 demonstrates that a moderate  $LoD_{crit}$  of 0.15 m already represents a limiting factor for the quantitative assessment.

#### 4.3.2 Probabilistic uncertainty assessments with UAV-SfM data

The analysis of the derived sediment budgets reveal limitations of probabilistic uncertainty assessments. Errors caused by georeferencing, SfM processing and GPS accuracy are propagated into the sediment budget, resulting in a high proportion of discarded sediment volumes. The applied  $LoD_{crit}$  of 0.15 m is in alignment with Wheaton et al. (2009) who worked with similar GCP densities and applied a  $LoD_{crit}$  of 0.1 m. Additionally, a review of other sediment budgeting campaigns with lower GCP densities and  $LoD_{crit} > 0.15$  m (Brasington et al., 2003; Croke et al., 2013; Dai et al., 2022; Lane et al., 2003) support the plausibility of the defined  $LoD_{crit}$  (see appendix B). This comparison underlines the importance of a sufficient GCP density for valuable sediment budgets. Conclusions drawn from accuracy assessments of DEM (Gindraux et al., 2017) question the globally applied  $LoD_{crit}$ , especially for UAV data with the low GCP densities (eBee Plus flights in 2020). The elevation error obtained from SfM processing reports also point towards a higher  $LoD_{crit}$  for point cloud derived from eBee Plus flights. Lacking availability of validation targets hinder a quantitative assessment of  $SDE_z$  for the concerning flights. However, former research provided supportive evidence that the defined  $LoD_{crit}$  is plausible: Flükiger (2022) also estimated a  $LoD_{crit}$  of 0.15 m for a DoD based on the identical UAV data.

#### 4.3.3 2D habitat change map as intermediate result

Before the estimated  $LoD_{crit}$  was applied, valid terrestrial sediment areas were determined by a 2D habitat change analysis showing morphological change of sediment habitats between the given time steps (Figure 10). The maps exhibited useful information about major sediment processes such as erosion and deposition, although it did not reach the same spatial resolution as achieved by Casado et al. (2015) or Scheib (2022). Additionally, minor patches and smaller island were missed by the 2D habitat change map which is a direct influence of CSF sediment classification (discussed in Section 4.1). Another limitation represented the narrowed focus on sediment and water bodies. This can introduce incorrect habitat classification. For instance, terrestrial sediment which is overtaken by vegetation growth would be classified as new erosion. This underlines not only restricting factor of this intermediate result but also shows unused potential for further development. An incorporation of the class *vegetation* would enhance the quality of 2D habitat change maps significantly.

#### 4.3.4 Significance assessment of propagated uncertainty

As proposed by Brasington et al. (2003) and Lane et al. (2003), the significance of the propagated uncertainties was assessed showing that lost sediment volumes ranged between 8.37 - 44.69 % for erosion and 9.05 - 58.83 % for deposition. Compared to other probabilistic sediment budget campaigns, this significance is similar to findings made by Lane et al. (2003) observed with airborne LiDAR and by Wheaton et al. (2009) observed with a total station (see appendix B). It is important to note that the resulting significance are influenced by multiple factors such as GCP density, acquisition method, spatial extent but also observed elevation changes. In the context of artificial floods, these elevation changes are linked to the flood parameters magnitude and duration. This influence becomes evident when the investigated floods are compared. The lowest significance was achieved when the smallest flood was encountered (2022). However, the achieved significance confirmed that terrestrial sediment budget based on point cloud derived from UAV-SfM data are able to deliver satisfactory results compared to established methods.

## 5 Conclusion and Outlook

With the quantitative assessment of terrestrial sediment volumes based on point cloud classification, the workflow developed in this master thesis supports prospective mitigation measures along hydropower-regulated rivers. In the context of artificial flooding, the generated results deliver not only the total amount of quantified terrestrial volumes. With an ECD and 2D habitat change map valuable information about the flood impact is provided and can be interpreted. Different practitioners directly profit from quantified sediment budgets. On the one hand, hydrologist are able to estimate change points during artificial floods. For instance, the mobilization of coarser sediment or breaking up the armour layer can be estimated and compared to results obtained from ecohydrological simulations (Flükiger, 2022). Furthermore, obtained sediment volumes can also be used as one input parameter of such ecohydrological numerical models. On the other hand, results of the developed workflow can be presented to hydropower managers and political stakeholders and contribute to the cost-effective planning of prospective floods.

The developed routines are capable of pre-process, filter and classify UAV or TLS point cloud data in effective and reproductive way. Furthermore, the developed scripts are written in free and open-source software which allows individual adoption, further development and poses an alternative to proprietary tools in this discipline. All relevant input parameters of the automated classification process can be adjusted in a configuration file (`.json`), outputs are generated in a structured and comprehensible way. Overall and as advocated by Vericat et al. (2017), the design properties of this tool contribute to a scalable, computer efficient and accessible software solution for sediment budgets of the future.

In addition to the presented results, the workflow has further potential. First, the investigated sediment volumes could be extended to submerged bodies to deliver a more holistic assessment method. This could be integrated with: (i) a refraction correction of the UAV-SfM data (Lane et al., 2020; Woodget et al., 2015), (ii) the use of specific airborne LiDAR with a water penetrating laser (Mandlburger et al., 2015), (iii) the combination with an acoustic doppler current profiler as examined by Milan & Heritage (2012). Second, the habitat change analysis could be further improved by a more comprehensive classification of low vegetation, since analysis focused on terrestrial sediment (Table 4). The chosen definition neglects other phenomena such as vegetation growth or different flow conditions. Partly, this issue could be addressed with the successful removal of mature vegetation (by CSF classification) but uncertain areas would remain. As a result, areas which are covered by a fine layer of pioneer vegetation were classified as *new erosion* and neglected by volume calculation. This could be done with the integration of RGB-based indices such as Green Leaf Index (GLI) or Excess Red Index (ERI) (Hunt et al., 2013; Meyer & Neto, 2008; Widłowski et al., 2000). First tests with TLS data showed promising results when  $GLI > 0.81$  or  $ERI > 0.92$  is applied. Third, this work treated DoD uncertainties spatially uniform, which ignores the different morpho-dynamic effects along a riverine system (Passalacqua et al., 2015; Vericat et al., 2017). For instance, shallow and widespread bank erosion caused by the minor flood in 2022 fall below  $LoD_{crit}$  and lead to a great loss of terrestrial sediment volumes. Spatially variable error estimation used by Wheaton et al. (2009) (with fuzzy inference system) or Lane et al. (2003) (zone dependent  $LoD_{crit}$ ) would be effective approaches to counter this limitation. Furthermore and as additional side-product, the refined classified point cloud data could be combined with audio recordings and then presented in virtual reality as awareness raising instrument (Wissen Hayek et al., 2023). Finally, the developed workflow emphasizes strengths and weakness of TLS and UAV data in different manner. Although each river shows different characteristics and challenges, the application of two separate surveys is indicated to emphasize the benefits of the developed workflow. For TLS, a bar to reach scale survey of a densely vegetated river is indicated. For UAV, a reach to network scale survey of a wide and braided gravel-bed river such as Tagliamento or Vjosa River represent an ideal study area to further enhance the workflow.

However, the implementation of artificial floods which contribute to the biodiversity along residual flow sections is not only determined by ecohydrological researchers and hydropower managers. An increased awareness of biodiversity loss among other stakeholders and the public is essential to improve the acceptance of such mitigation measures (Darwall et al., 2018). As one product of this work, classified point cloud environments presented in virtual reality may play a key role: the visualization of affected river sections with virtual reality goggles raises the awareness of biodiversity loss (Wissen Hayek et al., 2023) and would allow to exhibit positive changes after an artificial flood. Such immersive experiences may enable political stakeholders to find a more sustainable trade-off between energy production and ecological effects.

## References

- Antonetti, M., Buss, R., Scherrer, S., Margreth, M., & Zappa, M. (2016). Mapping dominant runoff processes: An evaluation of different approaches using similarity measures and synthetic runoff simulations. *Hydrology and Earth System Sciences*, 20(7), 2929–2945. <https://doi.org/10.5194/hess-20-2929-2016>
- Bailey, G., Li, Y., McKinney, N., Yoder, D., Wright, W., & Herrero, H. (2022). Comparison of Ground Point Filtering Algorithms for High-Density Point Clouds Collected by Terrestrial LiDAR. *Remote Sensing*, 14(19), 4776. <https://doi.org/10.3390/rs14194776>
- Berendsen, H. J. A., Stouthamer, E., & Berendsen, H. J. A. (2001). *Palaeogeographic development of the Rhine-Meuse delta, The Netherlands*. Koninklijke Van Gorcum. [https://doi.org/10.1046/j.1365-3091.2002.00469\\_1.x](https://doi.org/10.1046/j.1365-3091.2002.00469_1.x)
- Berkemeier, T., Ammann, M., Krieger, U. K., Peter, T., Spichtinger, P., Pöschl, U., Shiraiwa, M., & Huisman, A. J. (2017). Technical note: Monte Carlo genetic algorithm (MCGA) for model analysis of multiphase chemical kinetics to determine transport and reaction rate coefficients using multiple experimental data sets. *Atmospheric Chemistry and Physics*, 17(12), 8021–8029. <https://doi.org/10.5194/acp-17-8021-2017>
- Brasington, J., Langham, J., & Rumsby, B. (2003). Methodological sensitivity of morphometric estimates of coarse fluvial sediment transport. *Geomorphology*, 53(3-4), 299–316. [https://doi.org/10.1016/S0169-555X\(02\)00320-3](https://doi.org/10.1016/S0169-555X(02)00320-3)
- Brasington, J., Rumsby, B. T., & McVey, R. A. (2000). Monitoring and modelling morphological change in a braided gravel-bed river using high resolution GPS-based survey. *Earth Surface Processes and Landforms*, 25(9), 973–990. [https://doi.org/10.1002/1096-9837\(200008\)25:9%3C973::AID-ESP111%3E3.0.CO;2-Y](https://doi.org/10.1002/1096-9837(200008)25:9%3C973::AID-ESP111%3E3.0.CO;2-Y)
- Brasington, J., Vericat, D., & Rychkov, I. (2012). Modeling river bed morphology, roughness, and surface sedimentology using high resolution terrestrial laser scanning. *Water Resources Research*, 48(11). <https://doi.org/10.1029/2012WR012223>
- Brewer, P. A., & Passmore, D. G. (2002). Sediment budgeting techniques in gravel-bed rivers. *Geological Society, London, Special Publications*, 191(1), 97–113. <https://doi.org/10.1144/GSL.SP.2002.191.01.07>
- Brieger, F., Herzschuh, U., Pestryakova, L. A., Bookhagen, B., Zakharov, E. S., & Kruse, S. (2019). Advances in the Derivation of Northeast Siberian Forest Metrics Using High-Resolution UAV-Based Photogrammetric Point Clouds. *Remote Sensing*, 11(12), 1447. <https://doi.org/10.3390/rs11121447>
- Brown, A. G., Carey, C., Erkens, G., Fuchs, M., Hoffmann, T., Macaire, J.-J., Moldenhauer, K.-M., & Walling, D. E. (2009). From sedimentary records to sediment budgets: Multiple approaches to catchment sediment flux. *Geomorphology*, 108(1-2), 35–47. <https://doi.org/10.1016/j.geomorph.2008.01.021>
- Bunn, S. E., & Arthington, A. H. (2002). Basic Principles and Ecological Consequences of Altered Flow Regimes for Aquatic Biodiversity. *Environmental Management*, 30(4), 492–507. <https://doi.org/10.1007/s00267-002-2737-0>
- Callow, J. N., May, S. M., & Leopold, M. (2018). Drone photogrammetry and KMeans point cloud filtering to create high resolution topographic and inundation models of coastal sediment archives: Drone photogrammetry point cloud filtering. *Earth Surface Processes and Landforms*, 43(12), 2603–2615. <https://doi.org/10.1002/esp.4419>
- Carvalho, R. C., & Reef, R. (2022). Quantification of Coastal Change and Preliminary Sediment Budget Calculation Using SfM Photogrammetry and Archival Aerial Imagery. *Geosciences*, 12(10), 357. <https://doi.org/10.3390/geosciences12100357>
- Casado, M., Gonzalez, R., Kriechbaumer, T., & Veal, A. (2015). Automated Identification of River Hydromorphological Features Using UAV High Resolution Aerial Imagery. *Sensors*, 15(11), 27969–27989. <https://doi.org/10.3390/s151127969>
- Cavalli, M., Tarolli, P., Marchi, L., & Dalla Fontana, G. (2008). The effectiveness of airborne LiDAR data in the recognition of channel-bed morphology. *CATENA*, 73(3), 249–260. <https://doi.org/10.1016/j.catena.2007.11.001>
- Clapuyt, F., Vanacker, V., Schlunegger, F., & Van Oost, K. (2017). Unravelling earth flow dynamics with 3-D time series derived from UAV-SfM models. *Earth Surface Dynamics*, 5(4), 791–806. <https://doi.org/10.5194/esurf-5-791-2017>
- cloudcompare.org. (2023). *SOR filter - CloudCompare Wiki*. <https://www.cloudcompare.org/doc/wiki/index>.

- php?title=SOR\_filter
- Cohen, J. (1960). A Coefficient of Agreement for Nominal Scales. *Educational and Psychological Measurement*, 20(1), 37–46. <https://doi.org/10.1177/001316446002000104>
- Conesa-García, C., Puig-Mengual, C., Riquelme, A., Tomás, R., Martínez-Capel, F., García-Lorenzo, R., Pastor, J. L., Pérez-Cutillas, P., & Cano Gonzalez, M. (2020). Combining SfM Photogrammetry and Terrestrial Laser Scanning to Assess Event-Scale Sediment Budgets along a Gravel-Bed Ephemeral Stream. *Remote Sensing*, 12(21), 3624. <https://doi.org/10.3390/rs12213624>
- Croke, J., Todd, P., Thompson, C., Watson, F., Denham, R., & Khanal, G. (2013). The use of multi temporal LiDAR to assess basin-scale erosion and deposition following the catastrophic January 2011 Lockyer flood, SE Queensland, Australia. *Geomorphology*, 184, 111–126. <https://doi.org/10.1016/j.geomorph.2012.11.023>
- Dai, W., Qian, W., Liu, A., Wang, C., Yang, X., Hu, G., & Tang, G. (2022). Monitoring and modeling sediment transport in space in small loess catchments using UAV-SfM photogrammetry. *CATENA*, 214, 106244. <https://doi.org/10.1016/j.catena.2022.106244>
- Darwall, W., Bremerich, V., De Wever, A., Dell, A. I., Freyhof, J., Gessner, M. O., Grossart, H.-P., Harrison, I., Irvine, K., Jähnig, S. C., Jeschke, J. M., Lee, J. J., Lu, C., Lewandowska, A. M., Monaghan, M. T., Nejstgaard, J. C., Patricio, H., Schmidt-Kloiber, A., Stuart, S. N., ... Weyl, O. (2018). The Alliance for Freshwater Life : A global call to unite efforts for freshwater biodiversity science and conservation. *Aquatic Conservation: Marine and Freshwater Ecosystems*, 28(4), 1015–1022. <https://doi.org/10.1002/aqc.2958>
- Döring, M., Tonolla, D., Robinson, C. T., Schleiss, A., Stähly, S., Gufler, C., Geilhausen, M., & Di Cugno, N. (2018). *Künstliches Hochwasser an der Saane: eine Massnahme zum nachhaltigen Auenmanagement.* <https://doi.org/10.21256/ZHAW-2040>
- Eltner, A., Baumgart, P., Maas, H.-G., & Faust, D. (2015). Multi-temporal UAV data for automatic measurement of rill and interrill erosion on loess soil. *Earth Surface Processes and Landforms*, 40(6), 741–755. <https://doi.org/10.1002/esp.3673>
- Eltner, A., Kaiser, A., Castillo, C., Rock, G., Neugirg, F., & Abellán, A. (2016). Image-based surface reconstruction in geomorphometry – merits, limits and developments. *Earth Surface Dynamics*, 4(2), 359–389. <https://doi.org/10.5194/esurf-4-359-2016>
- Eltner, A., Mulsow, C., & Maas, H. G. (2013). Quantitative measurement of soil erosion from TLS and UAV data. *Int. Arch. Photogramm. Remote Sens. Spat. Inf. Sci*, 40, 4–6. <https://doi.org/10.5194/isprarchives-XL-1-W2-119-2013>
- Ely, J. C., Graham, C., Barr, I. D., Rea, B. R., Spagnolo, M., & Evans, J. (2017). Using UAV acquired photography and structure from motion techniques for studying glacier landforms: Application to the glacial flutes at Isfallsglaciären: UAV acquired photography for studying glacier landforms. *Earth Surface Processes and Landforms*, 42(6), 877–888. <https://doi.org/10.1002/esp.4044>
- Federal Office of Topography swisstopo. (2023). *swissTLM3D*. Bundesamt für Landestopografie swisstopo. <https://www.swisstopo.admin.ch/de/geodata/landscape/tlm3d.html>
- Flükiger, N. (2022). *Modelling ecomorphological effects of experimental floods in a complex floodplain* [Master Thesis]. Universität Basel. Ecohydrology Research Group, Zurich University of Applied Sciences.
- Ganssen, R., & Gračanin, Z. (1972). *Bodengeographie: Mit besonderer Berücksichtigung der Böden Mitteleuropas*. Verlag K. F. Koehler. <https://openlibrary.org/books/OL5490935M/Bodengeographie>
- Gindraux, S., Boesch, R., & Farinotti, D. (2017). Accuracy Assessment of Digital Surface Models from Unmanned Aerial Vehicles' Imagery on Glaciers. *Remote Sensing*, 9(2), 186. <https://doi.org/10.3390/rs9020186>
- Habersack, H., Wagner, B., Schoder, A., & Hauer, C. (2013). Die Bedeutung von Feststoffhaushalt und Sedimentdurchgängigkeit für eine nachhaltige Nutzung der Wasserkraft. *Österreichische Wasser- und Abfallwirtschaft*, 65(9-10), 354–361. <https://doi.org/10.1007/s00506-013-0108-0>
- Hijmans, R. J., Bivand, R., Pebesma, E., & Sumner, M. D. (2023). *Terra: Spatial Data Analysis* (Version 1.7-29) [Computer software]. <https://cran.r-project.org/web/packages/terra/index.html>
- Hijmans, R. J., Etten, J. van, Sumner, M., Cheng, J., Baston, D., Bevan, A., Bivand, R., Busetto, L., Canty, M., Fasoli, B., Forrest, D., Ghosh, A., Golicher, D., Gray, J., Greenberg, J. A., Hiemstra, P., Hingee, K., Illich, A., Geosciences, I. for M. A., ... Wueest, R. (2023). *Raster: Geographic Data Analysis and Modeling* (Version 3.6-20) [Computer software]. <https://cran.r-project.org/web/packages/raster/index.html>
- Hodge, R., Brasington, J., & Richards, K. (2009). In situ characterization of grain-scale fluvial morphology

- using Terrestrial Laser Scanning. *Earth Surface Processes and Landforms*, 34(7), 954–968. <https://doi.org/10.1002/esp.1780>
- Hoffmann, T., Erkens, G., Cohen, K. M., Houben, P., Seidel, J., & Dikau, R. (2007). Holocene floodplain sediment storage and hillslope erosion within the Rhine catchment. *The Holocene*, 17(1), 105–118. <https://doi.org/10.1177/0959683607073287>
- Höfle, B., Vetter, M., Pfeifer, N., Mandlburger, G., & Stötter, J. (2009). Water surface mapping from airborne laser scanning using signal intensity and elevation data. *Earth Surface Processes and Landforms*, 34(12), 1635–1649. <https://doi.org/10.1002/esp.1853>
- Houben, P., Hoffmann, T., Zimmermann, A., & Dikau, R. (2006). Land use and climatic impacts on the Rhine system (RheinLUCIFS): Quantifying sediment fluxes and human impact with available data. *CATENA*, 66(1-2), 42–52. <https://doi.org/10.1016/j.catena.2005.07.009>
- Hunt, E. R., & Daughtry, C. S. T. (2018). What good are unmanned aircraft systems for agricultural remote sensing and precision agriculture? *International Journal of Remote Sensing*, 39(15-16), 5345–5376. <https://doi.org/10.1080/01431161.2017.1410300>
- Hunt, E. R., Doraiswamy, P. C., McMurtrey, J. E., Daughtry, C. S. T., Perry, E. M., & Akhmedov, B. (2013). A visible band index for remote sensing leaf chlorophyll content at the canopy scale. *International Journal of Applied Earth Observation and Geoinformation*, 21, 103–112. <https://doi.org/10.1016/j.jag.2012.07.020>
- Kastenhofer, O. (2022). Long-term functional responses of macroinvertebrates to experimental floods and climate driven alterations in alpine streams. <https://doi.org/10.21256/ZHAW-25203>
- Landis, J. R., & Koch, G. G. (1977). An Application of Hierarchical Kappa-type Statistics in the Assessment of Majority Agreement among Multiple Observers. *Biometrics*, 33(2), 363. <https://doi.org/10.2307/2529786>
- Lane, S. N., Gentile, A., & Goldenschue, L. (2020). Combining UAV-Based SfM-MVS Photogrammetry with Conventional Monitoring to Set Environmental Flows: Modifying Dam Flushing Flows to Improve Alpine Stream Habitat. *Remote Sensing*, 12(23), 3868. <https://doi.org/10.3390/rs12233868>
- Lane, S. N., Westaway, R. M., & Murray Hicks, D. (2003). Estimation of erosion and deposition volumes in a large, gravel-bed, braided river using synoptic remote sensing. *Earth Surface Processes and Landforms: The Journal of the British Geomorphological Research Group*, 28(3), 249–271. <https://doi.org/10.1002/esp.483>
- Lang, M. W., & McCarty, G. W. (2009). Lidar intensity for improved detection of inundation below the forest canopy. *Wetlands*, 29(4), 1166–1178. <https://doi.org/10.1672/08-197.1>
- Legleiter, C. J. (2012). Remote measurement of river morphology via fusion of LiDAR topography and spectrally based bathymetry. *Earth Surface Processes and Landforms*, 37(5), 499–518. <https://doi.org/10.1002/esp.2262>
- Macaire, J.-J., Bernard, J., Di-Giovanni, C., Hinschberger, F., Limondin-Lozouet, N., & Visset, L. (2006). Quantification and regulation of organic and mineral sedimentation in a late-Holocene floodplain as a result of climatic and human impacts (Taligny marsh, Parisian Basin, France). *The Holocene*, 16(5), 647–660. <https://doi.org/10.1191/0959683606hl961rp>
- Maddock, I., Harby, A., Kemp, P., & Wood, P. (Eds.). (2013). *Ecohydraulics: An Integrated Approach* (1st ed.). Wiley. <https://doi.org/10.1002/9781118526576>
- Malinowski, R., Heckrath, G., Rybicki, M., & Eltner, A. (2023). Mapping rill soil erosion in agricultural fields with UAV-borne remote sensing data. *Earth Surface Processes and Landforms*, 48(3), 596–612. <https://doi.org/10.1002/esp.5505>
- Mandlburger, G., Hauer, C., Wieser, M., & Pfeifer, N. (2015). Topo-Bathymetric LiDAR for Monitoring River Morphodynamics and Instream Habitats—A Case Study at the Pielach River. *Remote Sensing*, 7(5), 6160–6195. <https://doi.org/10.3390/rs70506160>
- Meyer, G. E., & Neto, J. C. (2008). Verification of color vegetation indices for automated crop imaging applications. *Computers and Electronics in Agriculture*, 63(2), 282–293. <https://doi.org/10.1016/j.compag.2008.03.009>
- Milan, D. J., & Heritage, G. L. (2012). LiDAR and ADCP Use in Gravel-Bed Rivers: Advances Since GBR6. In M. Church, P. M. Biron, & A. G. Roy (Eds.), *Gravel-Bed Rivers* (1st ed., pp. 286–302). Wiley. <https://doi.org/10.1002/9781119952497.ch22>
- Milan, D. J., Heritage, G. L., & Hetherington, D. (2007). Application of a 3D laser scanner in the assessment of erosion and deposition volumes and channel change in a proglacial river. *Earth Surface Processes and*

- Landforms*, 32(11), 1657–1674. <https://doi.org/10.1002/esp.1592>
- Milne, J. A., & Sear, D. A. (1997). Modelling river channel topography using GIS. *International Journal of Geographical Information Science*, 11(5), 499–519. <https://doi.org/10.1080/136588197242275>
- Morsy, S. (2017). *Land/water discrimination and land cover classification using multispectral airborne lidar data* [PhD thesis]. Ryerson University Toronto, ON, Canada.
- Morsy, S., Shaker, A., El-Rabbany, A., & LaRocque, P. E. (2016). Airborne multispectral LiDAR data for land-cover classification and land/water mapping using different spectral indexes. *ISPRS Annals of the Photogrammetry, Remote Sensing and Spatial Information Sciences*, III-3, 217–224. <https://doi.org/10.5194/isprs-annals-III-3-217-2016>
- National Ecological Observatory Network. (2023). *The Basics of LiDAR - Light Detection and Ranging - Remote Sensing / NSF NEON / Open Data to Understand our Ecosystems*. <https://www.neonscience.org/resources/learning-hub/tutorials/lidar-basics>
- Passalacqua, P., Belmont, P., Staley, D. M., Simley, J. D., Arrowsmith, J. R., Bode, C. A., Crosby, C., DeLong, S. B., Glenn, N. F., Kelly, S. A., Lague, D., Sangireddy, H., Schaffrath, K., Tarboton, D. G., Wasklewicz, T., & Wheaton, J. M. (2015). Analyzing high resolution topography for advancing the understanding of mass and energy transfer through landscapes: A review. *Earth-Science Reviews*, 148, 174–193. <https://doi.org/10.1016/j.earscirev.2015.05.012>
- Pebesma, E. (2018). Simple Features for R: Standardized Support for Spatial Vector Data. *The R Journal*, 10(1), 439. <https://doi.org/10.32614/RJ-2018-009>
- Pix4D S.A. (2023). *PIX4Dmapper: Professional photogrammetry software for drone mapping*. Pix4D. <https://www.pix4d.com/product/pix4dmapper-photogrammetry-software>
- RIEGL Laser Measurement Systems GmbH. (2023). *RIEGL - RiSCAN PRO*. <http://www.riegl.com/products/software-packages/riscan-pro/>
- Robinson, C. T., Siebers, A. R., & Ortlepp, J. (2018). Long-term ecological responses of the River Spöl to experimental floods. *Freshwater Science*, 37(3), 433–447. <https://doi.org/10.1086/699481>
- Rotnicka, J., Dłużewski, M., Dąbski, M., Rodzewicz, M., Włodarski, W., & Zmarz, A. (2020). Accuracy of the UAV-Based DEM of Beach–Foredune Topography in Relation to Selected Morphometric Variables, Land Cover, and Multitemporal Sediment Budget. *Estuaries and Coasts*, 43(8), 1939–1955. <https://doi.org/10.1007/s12237-020-00752-x>
- Roussel, J. R., & Qi, J. (2018). RCSF: Airborne LiDAR Filtering Method Based on Cloth Simulation. *R Package Version*, 1(1).
- Roussel, J.-R., Auty, D., Coops, N. C., Tompalski, P., Goodbody, T. R. H., Meador, A. S., Bourdon, J.-F., de Boissieu, F., & Achim, A. (2020). lidR: An R package for analysis of Airborne Laser Scanning (ALS) data. *Remote Sensing of Environment*, 251, 112061. <https://doi.org/10.1016/j.rse.2020.112061>
- Sangireddy, H. (2011). *Point cloud classification for water surface identification in LiDAR datasets* [PhD thesis]. <http://hdl.handle.net/2152/ETD-UT-2011-05-3151>
- Scheib, M. (2022). *Künstliches Hochwasser an der Saane: Bewertung der Auswirkungen auf eine Aue von nationaler Bedeutung mittels Remote Sensing*. <https://doi.org/10.21256/ZHAW-26399>
- Schilling, S. (2023). *Development of an applied UAV-SFM Workflow for the Timber Volume Assessment of Coniferous Expansion in southwestern Montana* [Master Thesis]. Geoinformatics Research Group, Zurich University of Applied Sciences.
- Schwindt, S., Negreiros, B., Mudiaga-Ojemu, B. O., & Hassan, M. A. (2023). Meta-analysis of a large bedload transport rate dataset. *Geomorphology*, 435, 108748. <https://doi.org/10.1016/j.geomorph.2023.108748>
- Scrucca, L. (2013). GA: A Package for Genetic Algorithms in R. *Journal of Statistical Software*, 53(4). <https://doi.org/10.18637/jss.v053.i04>
- Sivanpillai, R., & Miller, S. N. (2010). Improvements in mapping water bodies using ASTER data. *Ecological Informatics*, 5(1), 73–78. <https://doi.org/10.1016/j.ecoinf.2009.09.013>
- Stähly, S., Franca, M. J., Robinson, C. T., & Schleiss, A. J. (2019). Sediment replenishment combined with an artificial flood improves river habitats downstream of a dam. *Scientific Reports*, 9(1), 5176. <https://doi.org/10.1038/s41598-019-41575-6>
- Tennekes, M. (2018). Tmap: Thematic Maps in R. *Journal of Statistical Software*, 84(6). <https://doi.org/10.18637/jss.v084.i06>

- Thoma, D. P., Gupta, S. C., Bauer, M. E., & Kirchoff, C. E. (2005). Airborne laser scanning for riverbank erosion assessment. *Remote Sensing of Environment*, 95(4), 493–501. <https://doi.org/10.1016/j.rse.2005.01.012>
- Thorp, J. H., Thoms, M. C., & Delong, M. D. (2008). *The riverine ecosystem synthesis: Toward conceptual cohesiveness in river science* (1st ed). Academic Press.
- Tockner, K., Bunn, S. E., Gordon, C., Naiman, R. J., Quinn, G. P., & Stanford, J. A. (2008). Flood plains: Critically threatened ecosystems. In N. V. C. Polunin (Ed.), *Aquatic Ecosystems* (1st ed., pp. 45–62). Cambridge University Press. <https://doi.org/10.1017/CBO9780511751790.006>
- Tonolla, D., Geilhausen, M., & Doering, M. (2021). Seven decades of hydrogeomorphological changes in a near-natural (Sense River) and a hydropower-regulated (Sarine River) pre-Alpine river floodplain in Western Switzerland. *Earth Surface Processes and Landforms*, 46(1), 252–266. <https://doi.org/10.1002/esp.5017>
- Trimble Incorporated. (2021). *Trimble R10 Model 2 GNSS System - Datasheet*.
- Vericat, D., Wheaton, J. M., & Brasington, J. (2017). Revisiting the Morphological Approach: Opportunities and Challenges with Repeat High-Resolution Topography. In D. Tsutsumi & J. B. Laronne (Eds.), *Gravel-Bed Rivers* (pp. 121–158). John Wiley & Sons, Ltd. <https://doi.org/10.1002/9781118971437.ch5>
- Ward, J. V., & Stanford, J. A. (1983). The serial discontinuity concept of lotic ecosystems. *Dynamics*, 29–42.
- Warrick, J. A., Bountry, J. A., East, A. E., Magirl, C. S., Randle, T. J., Gelfenbaum, G., Ritchie, A. C., Pess, G. R., Leung, V., & Duda, J. J. (2015). Large-scale dam removal on the Elwha River, Washington, USA: Source-to-sink sediment budget and synthesis. *Geomorphology*, 246, 729–750. <https://doi.org/10.1016/j.geomorph.2015.01.010>
- Westaway, R. M., Lane, S. N., & Hicks, D. M. (2001). Remote sensing of clear-water, shallow, gravel-bed rivers using digital photogrammetry. *Photogrammetric Engineering and Remote Sensing*, 67(11), 1271–1281.
- Westoby, M. J., Brasington, J., Glasser, N. F., Hambrey, M. J., & Reynolds, J. M. (2012). “Structure-from-Motion” photogrammetry: A low-cost, effective tool for geoscience applications. *Geomorphology*, 179, 300–314. <https://doi.org/10.1016/j.geomorph.2012.08.021>
- Westoby, M. J., Rounce, D. R., Shaw, T. E., Fyffe, C. L., Moore, P. L., Stewart, R. L., & Brock, B. W. (2020). Geomorphological evolution of a debris-covered glacier surface. *Earth Surface Processes and Landforms*, 45(14), 3431–3448. <https://doi.org/10.1002/esp.4973>
- Wheaton, J. M., Brasington, J., Darby, S. E., & Sear, D. A. (2009). Accounting for uncertainty in DEMs from repeat topographic surveys: Improved sediment budgets. *Earth Surface Processes and Landforms*, 35(2), 136–156. <https://doi.org/10.1002/esp.1886>
- Wickham, H., Averick, M., Bryan, J., Chang, W., McGowan, L., François, R., Grolemund, G., Hayes, A., Henry, L., Hester, J., Kuhn, M., Pedersen, T., Miller, E., Bache, S., Müller, K., Ooms, J., Robinson, D., Seidel, D., Spinu, V., ... Yutani, H. (2019). Welcome to the Tidyverse. *Journal of Open Source Software*, 4(43), 1686. <https://doi.org/10.21105/joss.01686>
- Widlowski, J.-L., Verstraete, M. M., Pinty, B., & Gobron, N. (2000). Advanced vegetation indices optimized for up-coming sensors: Design, performance, and applications. *IEEE Transactions on Geoscience and Remote Sensing*, 38(6), 2489–2505. <https://doi.org/10.1109/36.885197>
- Wilke, C. O. (2020). *Cowplot: Streamlined Plot Theme and Plot Annotations for 'Ggplot2'* (Version 1.1.1) [Computer software]. <https://cran.r-project.org/web/packages/cowplot/index.html>
- Wissen Hayek, U., Gutscher, F., Braune, P., Dantas, N., Roost, D., Schürch, J., Antonetti, M., Grêt Regamey, A., & Döring, M. (2023). *Sensing river and floodplain biodiversity: Developing a prototype*. <https://doi.org/10.21256/ZHAW-27938>
- Woodget, A. S., Carbonneau, P. E., Visser, F., & Maddock, I. P. (2015). Quantifying submerged fluvial topography using hyperspatial resolution UAS imagery and structure from motion photogrammetry. *Earth Surface Processes and Landforms*, 40(1), 47–64. <https://doi.org/10.1002/esp.3613>
- SR 814.20 - Federal Act of 24 January 1991 on the Protection of Waters, Pub. L. No. 814.20 (2023). [https://www.fedlex.admin.ch/eli/cc/1992/1860\\_1860\\_1860/en](https://www.fedlex.admin.ch/eli/cc/1992/1860_1860_1860/en)
- Yu, B., Liu, H., Wu, J., Hu, Y., & Zhang, L. (2010). Automated derivation of urban building density information using airborne LiDAR data and object-based method. *Landscape and Urban Planning*, 98(3-4), 210–219. <https://doi.org/10.1016/j.landurbplan.2010.08.004>
- Zhang, K., Chen, S.-C., D. Whitman, Shyu, M.-L., Yan, J., & Zhang, C. (2003). A progressive morphological filter for removing nonground measurements from airborne LIDAR data. *IEEE Transactions on Geoscience*

- and Remote Sensing*, 41(4), 872–882. <https://doi.org/10.1109/TGRS.2003.810682>
- Zhang, W., Qi, J., Wan, P., Wang, H., Xie, D., Wang, X., & Yan, G. (2016). An Easy-to-Use Airborne LiDAR Data Filtering Method Based on Cloth Simulation. *Remote Sensing*, 8(6), 501. <https://doi.org/10.3390/rs8060501>
- Zurwerra, A., Meile, T., & Käser, S. (2016). *Künstliche Hochwasser. Massnahme zur Beseitigung ökologischer Beeinträchtigungen in Restwasserstrecken unterhalb von Speicherseen. Auslegeordnung Grundlagen & Handlungsbedarf [Im Auftrag des BAFU]*. PRONAT & BG. [https://www.parc.ch/snp/mmd\\_fullentry.php?docu\\_id=33630](https://www.parc.ch/snp/mmd_fullentry.php?docu_id=33630)

## Appendix

**Appendix A:** Source code of developed workflow

**Appendix B:** Overview of probabilistic Sediment Budget publications

**Appendix C:** Uncertainty Assessment of TLS data 2022

**Appendix D:** Results derived from CSF classification routine based on TLS data

**Appendix E:** Results derived from CSF classification routine based on UAV data

**Appendix F:** Subsets of all validation targets used for the uncertainty assessment of TLS point cloud.

**Appendix G:** Results derived from sediment budget routine based on UAV data

**Appendix H:** Results derived from sediment budget routine based on TLS data

### Appendix A

Source code can be found under [https://github.com/gubely/pcc\\_standalone](https://github.com/gubely/pcc_standalone).

### Appendix B

Table 6: Detailed information of probabilistic Sediment Budget publications showing minimal and maximal values of GCP density, study area, critical level of detection (LoDcrit) and used confidence interval t (NA: not available)

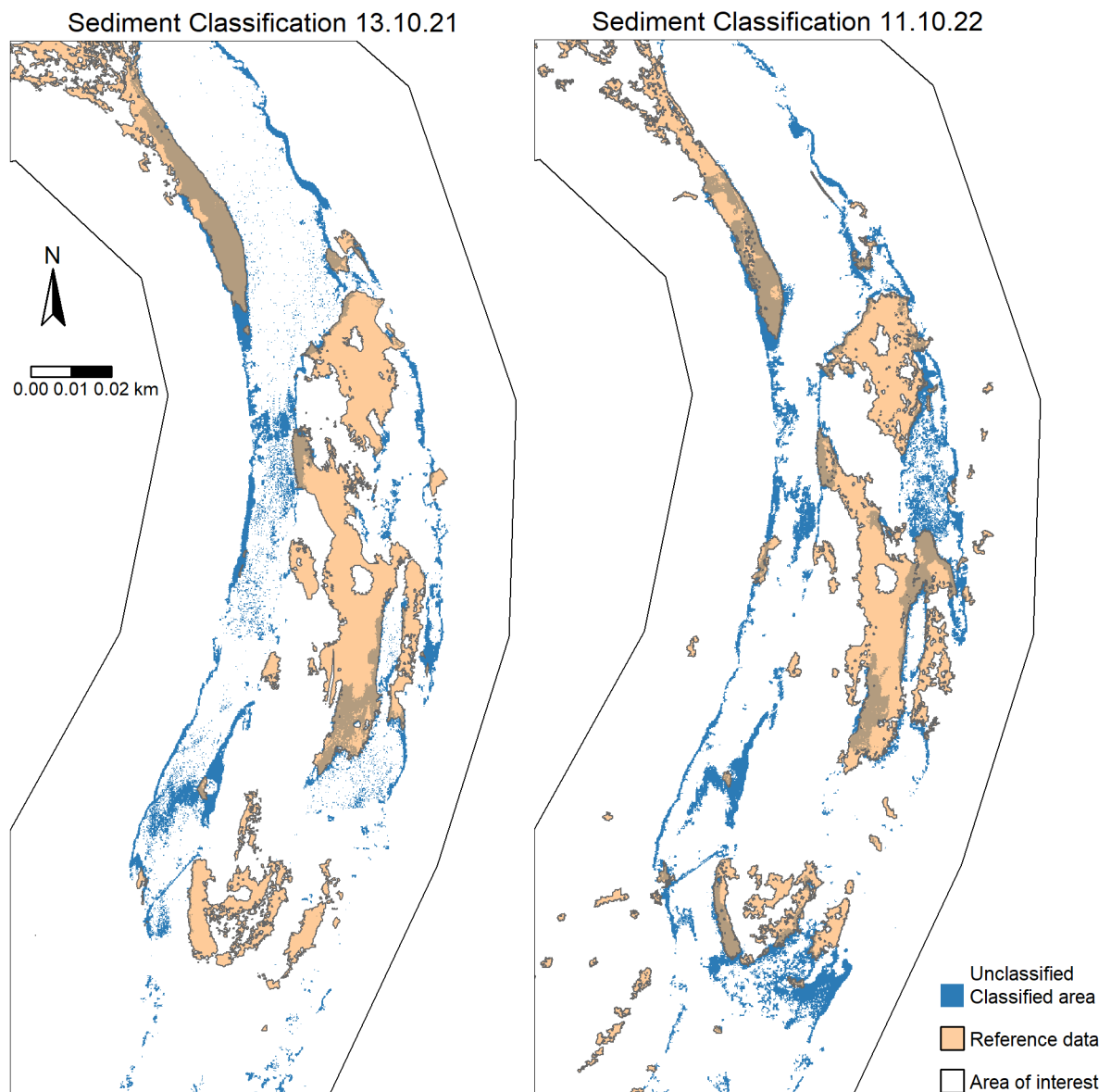
Author	GCP used	LoDcrit	Study area	GCP density	t
Milan et al. (2007)	20	0.057 - 0.133	0.005881	3389.8	2
Wheaton et al. (2009)	5 - 16	0.100	~ 0.14	35.7 - 114.3	2
Croke et al. (2013)	NA	0.400	~ 100	NA	2
Lane et al. (2003)	45	0.165 - 0.409	~ 3.3	13.6	1
Brasington et al. (2003)	15 - 20	0.410 - 0.804	~ 2	7.5 - 10	2
Dai et al. (2022)	24 - 34	0.166	0.108	222 - 314	2
Dai et al. (2022)	24 - 34	0.249	0.5046	47.5 - 67.3	2
Sarine UAV	4 - 14	0.15	0.081	49.4 - 172.8	2
Sarine TLS	6	0.18	0.0364 [m]	164.83 [km <sup>2</sup> ]	2 [sigma]

## Appendix C

Table 7: Manual uncertainty assessment of TLS data 2022 based on 27 validation targets whereas only 8 could be used due to restricted visibility. Coordinates stated in CH1903+ LV95.

ID	X (GPS)	Y (GPS)	Z (GPS)	Visibility	X (TLS)	Y (TLS)	Z (TLS)	$\Delta Z$
1	2575024.361	1178871.295	574.547	No				
2	2575055.086	1178843.519	574.914	No				
4	2575240.31	1178808.981	575.587	No				
5	2575311.388	1178815.044	576.086	No				
6	2575322.275	1178812.702	575.791	No				
7	2575352.44	1178792.377	575.97	No				
8	2575367.525	1178784.274	575.822	No				
9	2575384.571	1178748.35	575.738	No				
10	2575420.828	1178701.682	576.533	Ideal	2575420.852	1178701.691	576.51	0.023
11	2575427.038	1178683.266	576.984	Ideal	2575427.036	1178683.269	576.978	0.006
12	2575419.193	1178665.903	576.86	Fair	2575419.334	1178666.025	576.718	0.142
13	2575428.677	1178634.596	576.844	Fair	2575428.641	1178634.61	576.841	0.003
14	2575426.819	1178611.614	576.754	No				
15	2575399.141	1178568.789	577.124	No				
16	2575411.945	1178559.538	576.874	Good	2575411.977	1178559.565	576.8606	0.0134
17	2575391.54	1178552.673	576.753	No				
18	2575385.782	1178569.417	576.848	Poor	2575385.791	1178569.49	576.934	-0.086
19	2575404.74	1178623.263	577.42	No				
20	2575413.815	1178645.699	577.233	No				
21	2575420.874	1178646.935	577.344	Good	2575421.002	1178646.918	577.402	-0.058
22	2575436.754	1178655.9	576.222	Good	2575436.853	1178655.875	576.219	0.003
23	2575440.9	1178639.5	576.552	No				
24	2575410.878	1178681.243	575.982	No				
25	2575411.671	1178695.433	576.098	No				
26	2575420.325	1178725.16	575.684	No				
27	2575395.545	1178722.578	575.826	No				
28	2575367.064	1178770.287	576.105	No				
					Mean	0.0058		
					SDE	<b>0.0627</b>		
					[m]			

## Appendix D



## Appendix E

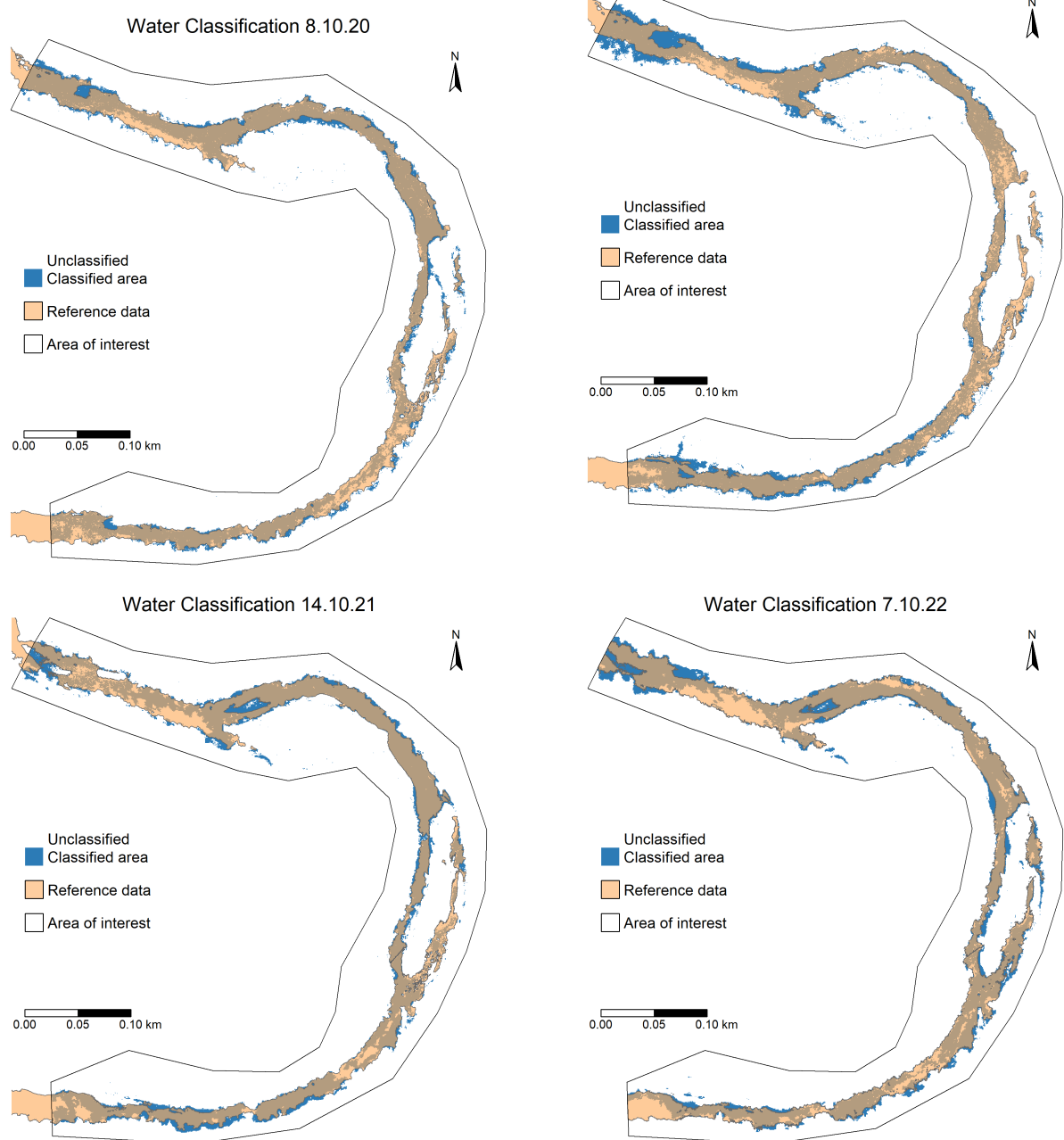


Figure 15: Results derived from CSF classification routine based on UAV data, showing classified water surface in blue and reference data in orange.

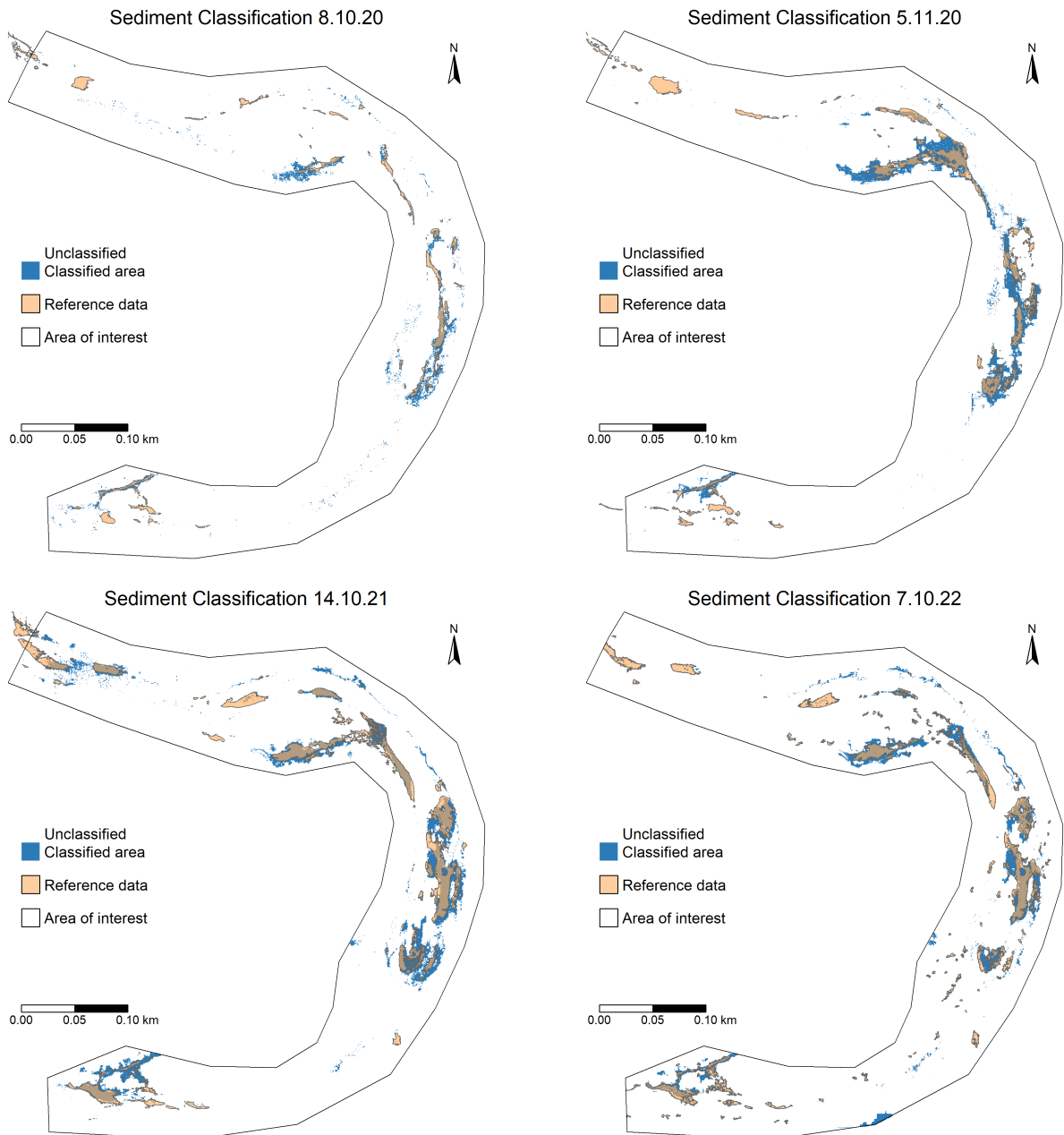
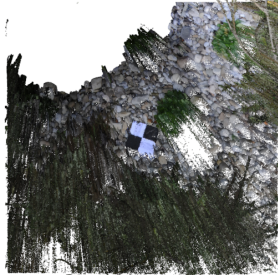


Figure 16: Results derived from CSF classification routine based on UAV data, showing classified terrestrial sediment in blue and reference data in orange.

**Appendix F**

(a) GCP 11



(b) GCP 10



(c) GCP 12



(d) GCP 13



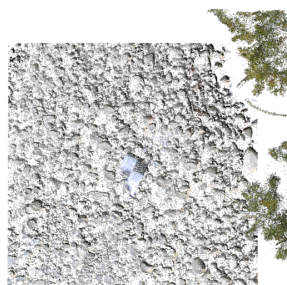
(e) GCP 16



(f) GCP 18



(g) GCP 21



(h) GCP 22

Figure 17: Subsets of all validation targets used for the uncertainty assessment of TLS point cloud.

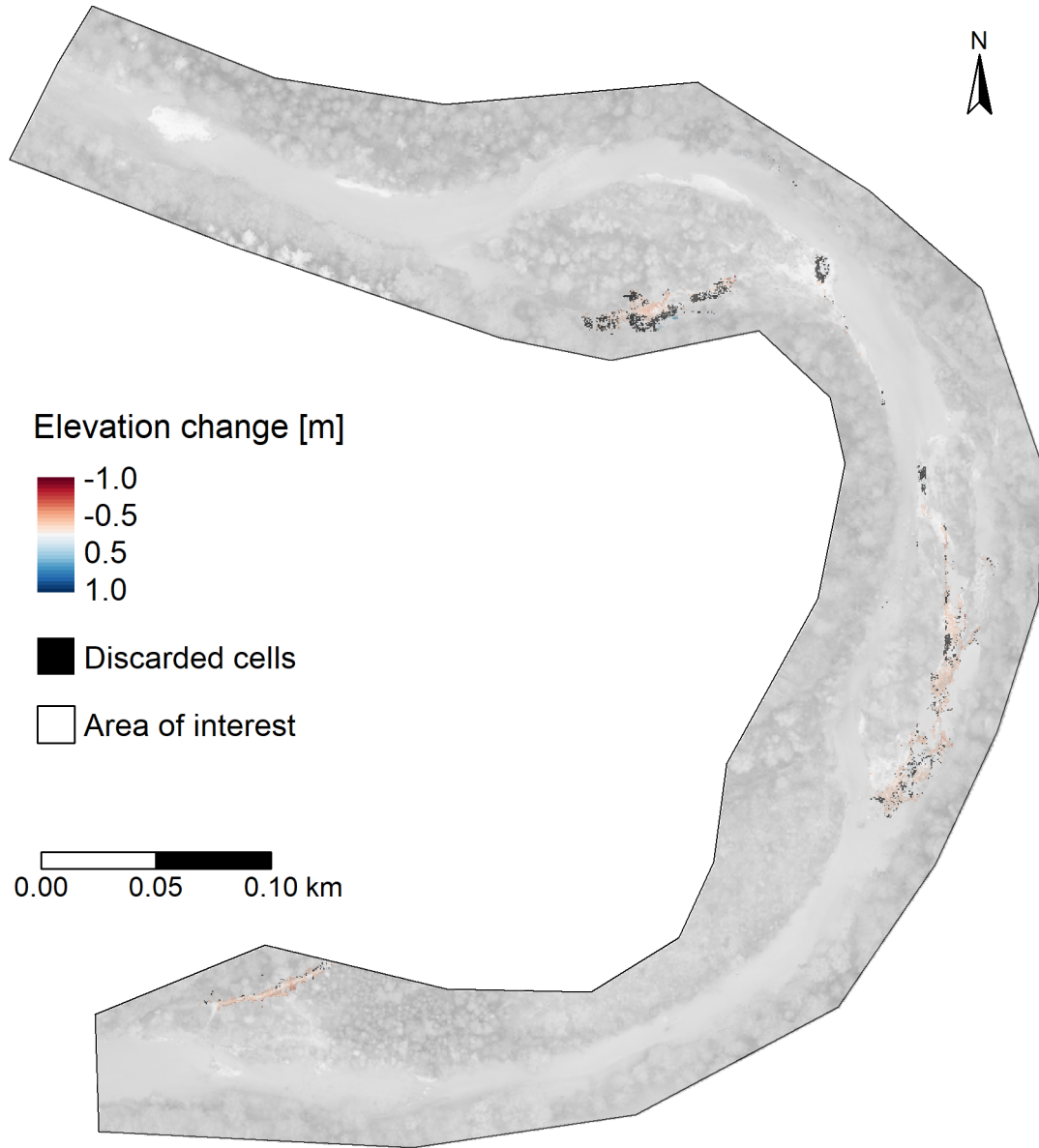
**Appendix G**

Figure 18: Derived sediment budget from the flood on 22.10.20, showing a elevation change map. Erosional elevation change is displayed in red, depositional in blue, elevation change below the critical level of detection (0.15 m) is displayed in black. (Source: Orthoimage after the flood event on the 8.10.2020 provided by the Ecohydrology research group).

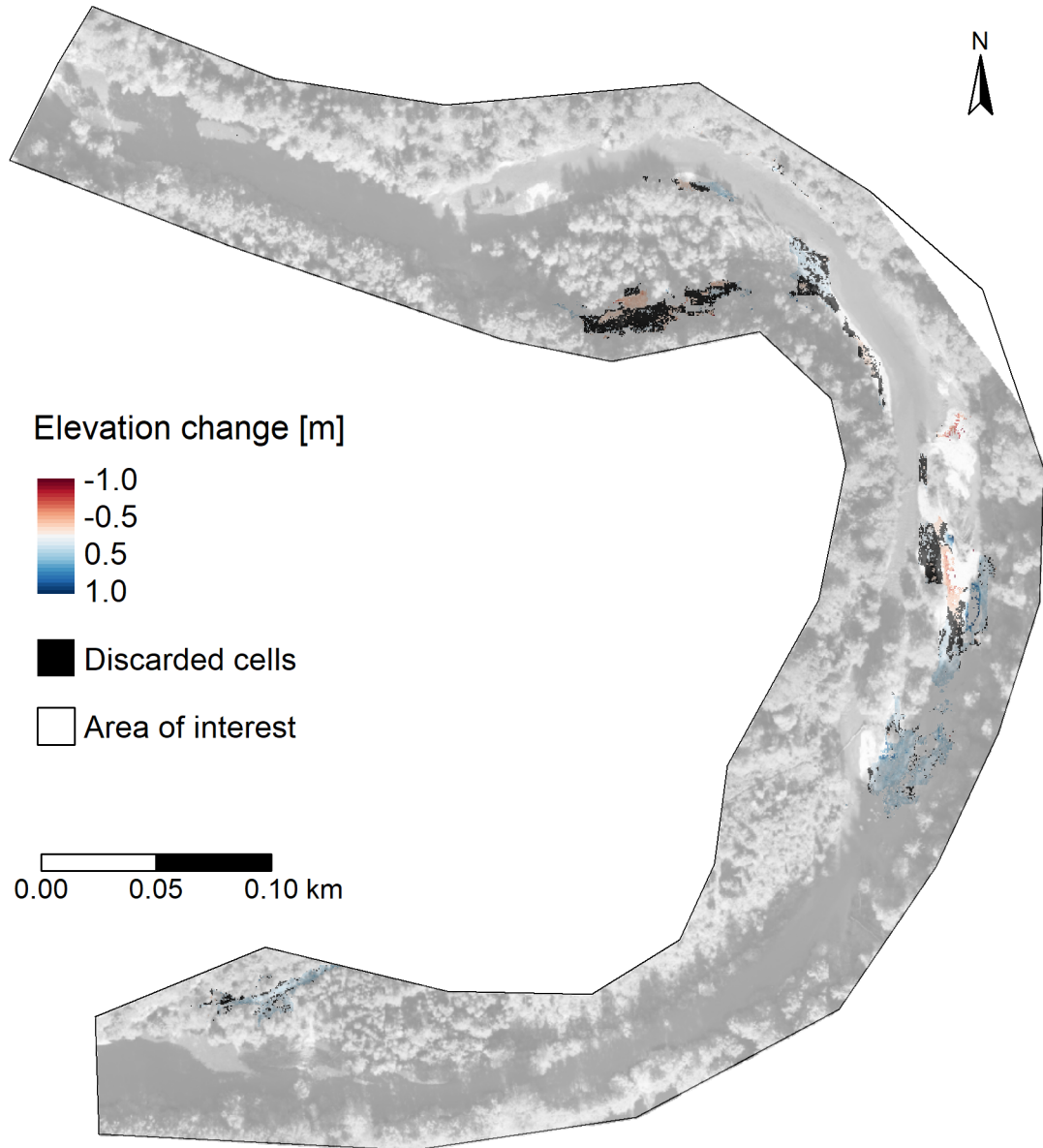


Figure 19: Derived sediment budget from the flood on 11.7.21, showing a elevation change map. Erosional elevation change is displayed in red, depositional in blue, elevation change below the critical level of detection ( $0.15\text{ m}$ ) is displayed in black. (Source: Orthoimage after the flood event on the 14.10.2021 provided by the Ecohydrology research group).

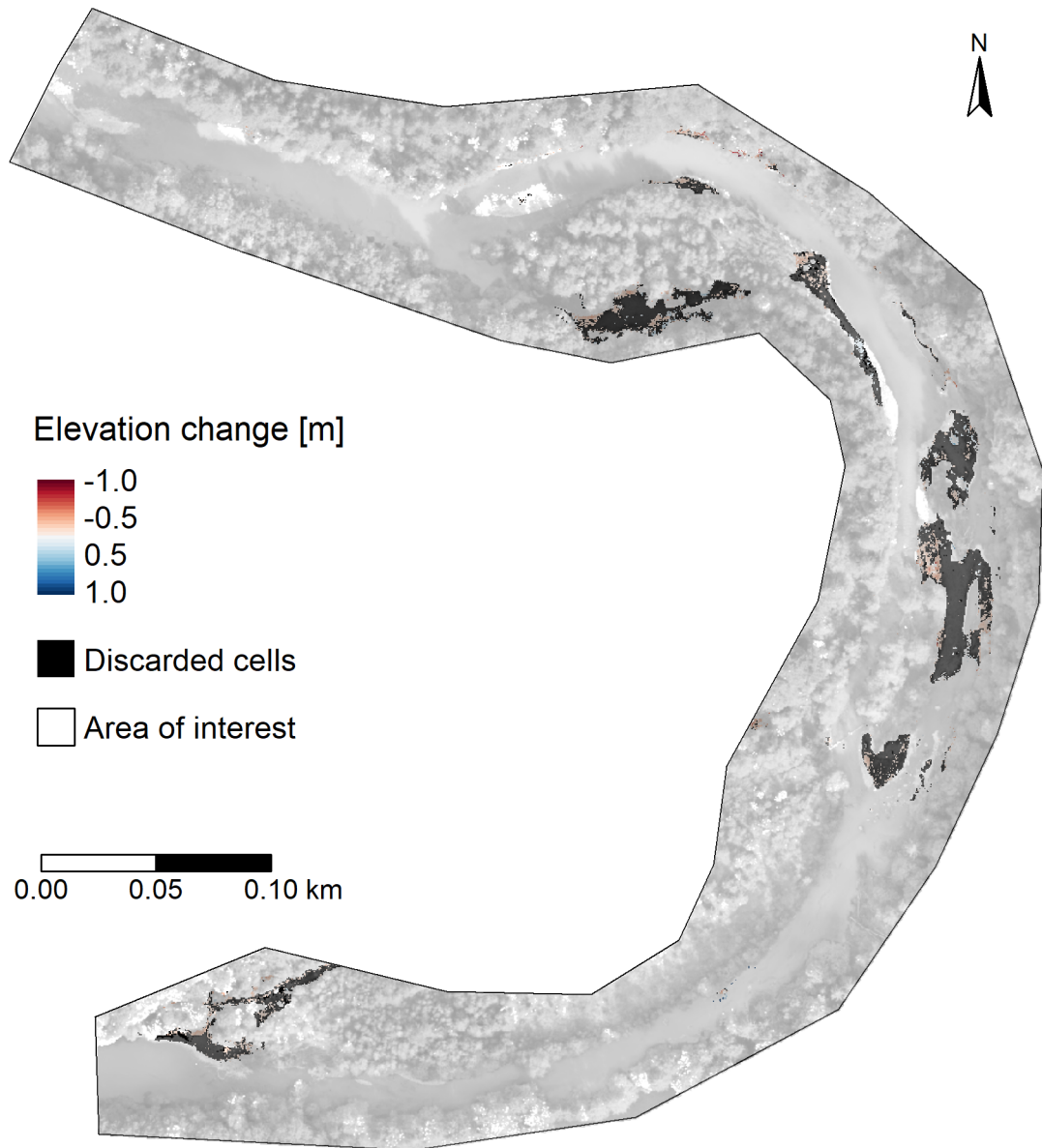


Figure 20: Derived sediment budget from the flood on the 31.5.2022, showing a elevation change map. Erosional elevation change is displayed in red, depositional in blue, elevation change below the critical level of detection (0.15 m) is displayed in black. (Source: Orthoimage after the flood event on the 7.10.2022 provided by the Ecohydrology research group).

## Appendix H

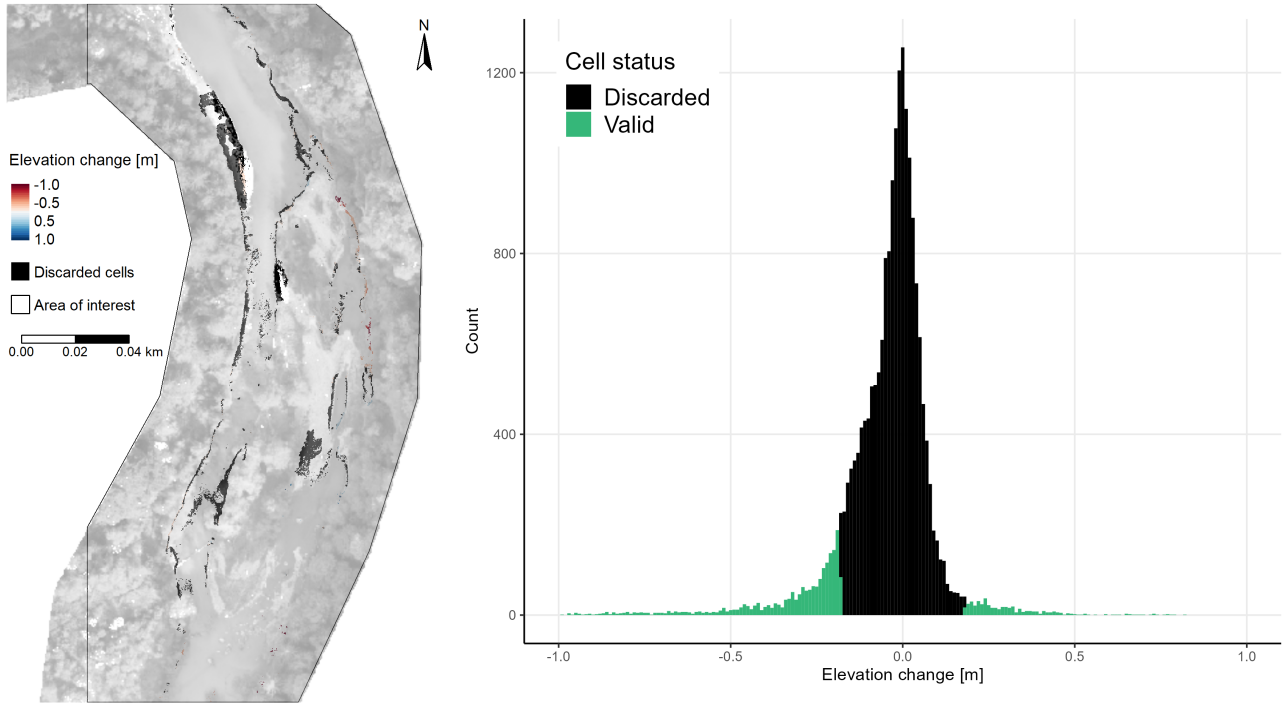


Figure 21: Derived sediment budgets from the flood on the 31.5.2022 based on TLS data, showing a digital elevation change map (left) and elevation change distribution (right). Erosional elevation change is displayed in red, depositional in blue, elevation change below the critical level of detection (0.18 m) is displayed in black. (Source: Orthoimages after the flood events on the 7.10.2022 provided by the Ecohydrology research group).

Table 8: Sediment budget results based on TLS data with a critical level of detection = 0.18 m.

Flood date	Deposited volume			Eroded volume				
	Valid	Total	Discarded	Zone Average	Valid	Total	Discarded	Zone Average
31.05.2022 Unit	6.64 [m <sup>3</sup> ]	18.82 [m <sup>3</sup> ]	64.74 [%]	0.346 [m <sup>3</sup> /m <sup>2</sup> ]	-33.34 [m <sup>3</sup> ]	-60.74 [m <sup>3</sup> ]	45.11 [%]	-0.409 [m <sup>3</sup> /m <sup>2</sup> ]